9

Computational Fluid Dynamics Analysis of Turbulent Flow

Pradip Majumdar
Department of Mechanical Engineering, Northern Illinois University, Illinois U.S.A

1. Introduction

One important characteristics of a turbulent flow is that the velocity and pressure may be steady or remain constant at a point, but still may exhibit irregular fluctuations over the mean or average value. The fluid elements which carry out fluctuations both in the direction of main flow and at right angles to flow are not individual molecules but rather are lumps of fluid of varying sizes known as eddies. The fluctuating components may be a few percent of the mean value, but it is the controlling factor in describing the flow. A turbulent fluid flow is then characterized as the main flow stream super-imposed with localized rotational eddies, where motion are three dimensional, unstable, and random. Turbulent eddies have a wide range of sizes or length scales. These eddies form continuously and disintegrate within few oscillation periods, and hence have very small time scales. In general, the frequencies of the unsteadiness and the size of the scales of motion span several orders of magnitude.

The governing equations for fluid flow for a general linear Newtonian viscous fluid are Navier-Stokes equations given by the following set of equations:

$$\frac{\partial \rho}{\partial t} + \frac{\partial}{\partial x_i}(\rho u_i) = 0 \tag{1}$$

$$\frac{D(\rho u_i)}{Dt} = \rho g - \nabla p + \frac{\partial}{\partial x_j}\left[\mu\left(\frac{\partial u_i}{\partial x_j} + \frac{\partial u_j}{\partial x_i}\right) + \delta_{ij}\lambda div V\right] \tag{2}$$

Where u_i and u_j are the mean velocities of water, P is the pressure, ρ is the density of the water and μ is the dynamic viscosity.

In principle, the time dependent three dimensional Navier-Stokes equations can fully describe all the physics of a given turbulent flow. This is due to the fact that turbulence is continuous process which consist of continuous spectrum of scales ranging from the largest one associated with the largest eddy to the smallest scales associated with the smallest eddy, referred as *Kolmogorov micro-scale*, a concept brought by the theory of turbulence statistics. These eddies overlap in space, larger one carrying the smaller ones. The process can be characterized as a cascading process by which the turbulence dissipates its kinetic energy from the larger eddies to the smaller eddies through vortex stretching. The energy is finally

dissipated into heat through the action of molecular viscosity in the smallest eddies. These larger eddies randomly stretch the vortex elements that compress the smaller eddies cascading energy to them. The cascading process give rise to the important features such as apparent stresses and enhanced diffusivity, which are several orders of magnitude larger than those in corresponding laminar flows. The scales of motion or wave lengths usually extend all the way from a maximum size comparable to the characteristic length of the flow channel to a minimum scale corresponding to the smallest eddy fixed by the viscous dissipation. The range of these scales or the ratio of minimum to maximum wave lengths varies with characteristic flow parameter such as Reynolds number of the flow.

2. Computational model for turbulence flow

In the computational simulation of turbulent flow, it is important to decide how finely we should resolve theses eddies in the computational model as it has a direct effect on the accuracy of the prediction as well as computer time. Methods available for simulating turbulent fluid flow are Direct *Numerical Simulation (DNS)* based on direct solution of Navier-Stokes Equations and *Averaged or Filtered Simulation* based on averaged solution of Navier-Stokes Equations. A brief description of these methods is described as follows:

2.1 Direct Numerical Simulation (DNS)

A computational model based on the micro-scale discretization is called Direct Numerical Simulation (DNS). It involves complete resolution of the flow field by a direct solution of unsteady Navier-Stokes Equations resolving all active scales of motion in the flow field without using any approximation and models. The grid spacing and time steps should be fine enough to capture the dynamics of all scales down to the smallest scale associated with the smallest eddy, which is established by the *Kolmogorov microscale*. The smallest eddy based on *Kolmogorov micro-scale* decreases with the increase in flow Reynolds number in proportion to the value of $Re^{9/4}$ and could be as small as 0.1-1 mm. Also, the computational domain should be large enough to include the largest scale of the flow dynamic, which is established by the characteristic dimension such as the height and width of the flow domain. Resolving all scales and frequencies of turbulent eddies based on the *Kolmogorov microscale* requires excessively large number of nodal points and excessively large computational time, and faces serious obstacles even with the most powerful supercomputers available today.

There are two basic requirements that a DNS model must meet to represent turbulence. These are: 1. It must represent a solution of Navier-Stokes equations resolving all scales of motion (viscous dissipation scales) adequately by the computational mesh, and 2. It should provide adequate statistical resolution (large samples or smaller time steps) of the set of all possible fluid motions allowed by the Navier-Stokes equations. These two requirements for a turbulence simulation conflict. The sample improves as the energy moves to smaller scales, but the viscous resolution is degraded. As a result, a DNS model of three-dimensional time dependent Navier-Stokes Equations for all important scales of turbulence has posed a great challenge for computer and numerical techniques in the past due to the requirement of extremely fine mesh size distribution and very small time steps to capture the essential details of the turbulent structures. Such requirements had limited the past DNS studies to very low Reynolds numbers. More detail descriptions of DNS method are given

by Eswaran and Pope (1988), Rai and Moin (1991, Kim et. al. (1997), Rogallo (1981) and Deb and Majumdar (1999).

2.2 Averaged or filtered simulation

In order to overcome the computational difficulties in terms grid size limitation imposed by *Kolmogorov microscale*, a simplified approach based on the solution of average Navier-Stokes Equations is most often used for turbulent fluid flow. An averaging or filtering operation is employed over the Navier-Stokes equation in order to smooth out certain range of high frequency variation of flow variables or smaller scales of turbulent eddies. This *averaging* or *filtering operation*, also known as *coarse graining* leads to a new set of flow governing equations that represents only the larger scale eddies or lower frequencies of flow variable. Because of the smoother variation of the flow variables, the smallest scale are no longer of the order of *Kolmogorov microscale*, but rather limited by the cut-off scale used in the averaging or filtering method and this results in a considerable reduction in the number of grid points and savings in computational time. So in the averaged or filtered simulation, only large scale of turbulence eddies are resolved, and an average affects of small scale eddies on the resolved scales are taken into account by the use of statistical average model, known as turbulence closure models. Turbulence modeling is designed to simulate the averaged flow Field, named as *coarse graining* instead of the original flow field. In this coarse graining process, small scale eddies that are difficult to resolve are neglected. The small eddies that are neglected in coarse graining are included in the simulation through the *turbulence modeling*.

Options available for analyzing turbulent flows are either a time-averaged approach using Reynolds Averaged Navier-Stokes (RANS) equations along with turbulence closure models, or a space-averaged approach using Large Eddy Simulations (LES) that takes into account of only large scale eddies and uses turbulence closure model for the smaller eddies, but require large amounts of computational time as well.

2.2.1 Large Eddy Simulation (LES)

In order avoid the limitation of the DNS method to resolve all scales of turbulence eddies in terms of smallest mesh size refinements, large eddy simulation (LES) are used. In large eddy simulation, the unsteady nature of turbulent eddies and only large scale eddies are resolved. The large scale eddies are anisotropic in nature and responsible for the driving physical mechanism such as production and major carrier of the turbulent kinetic energy. The small scale eddies are only responsible for viscous dissipation of small fraction of kinetic energy that they carry. The small scale eddies are modeled based on assuming an isotropic or a direction independent nature of eddies that follow a statistically predictive behavior for all turbulent flows. As small scale eddies are not resolved, LES methods are computationally less expansive than DNS method in which all scales or turbulence eddies are resolved. Nevertheless, LES method still requires finer mesh size distributions and computationally more expansive than RANS model.

2.2.2 Reynolds Averaged Navier-Stokes (RANS) model

Reynolds Averaged Navier-Stokes (RANS) model is the next level of approximation in which no attempts are made to resolve the unsteady nature of any sizes of turbulence

eddies. The increased level of mixing and dissipation caused by the turbulent eddies is taken into account through the turbulence closure models. In this approximation, the turbulence itself is not directly computed, but rather its average effect on mean flow is modeled by describing the turbulent motion in terms of time averaged form of Navier-Stokes equation referred to as the Reynolds-Averaged Navier-Stokes Equations. As described before instantaneous turbulent flow quantities are composed of two different types of motions: mean motion and a fluctuating motion as described by the following expressions for the instantaneous velocity components and pressure as

$$u = \bar{u} + u', v = \bar{v} + v', w = \bar{w} + w' \text{ and } p = \bar{p} + p' \tag{3}$$

The mean velocity components are represented as $\bar{u}$, $\bar{v}$ and $\bar{w}$. The fluctuating (time dependent) components u', v' and w', when added with the mean (time-independent) $\bar{u}$, $\bar{v}$ and $\bar{w}$ components gives the instantaneous velocity components. The time mean of a quantity ϕ is described as

$$\bar{\phi} \equiv \lim_{T\to\infty} \frac{1}{T} \int_{t_o}^{t_o+T} \phi \, dt \tag{4}$$

The velocity fluctuations produce mean rates of momentum transfer in addition to those produced by the mean velocity components. Substituting all fluctuating flow quantities given by equation (3) into in the Navier-Stokes equation (1-2) and performing the time averaged integration, the Reynolds-averaged Navier-Stokes equation is obtained as

$$\frac{\partial \rho}{\partial t} + \frac{\partial}{\partial x_i}(\rho u_i) = 0 \tag{5}$$

$$\frac{\partial}{\partial t}(\rho u_i) + \frac{\partial}{\partial x_j}(\rho u_i u_j - T_{ij}) = -\frac{\partial P}{\partial x_i} + \rho g_i + F_i \tag{6}$$

Where

$$T_{ij} = \left[\mu \left(\frac{\partial u_i}{\partial x_j} + \frac{\partial u_j}{\partial x_i} \right) \right] - \frac{2}{3}\mu \frac{\partial u_k}{\partial x_k} \delta_{ij} - \overline{\rho u_i' u_j'} \tag{7}$$

The time averaged Navier-Stokes equation is complicated by the inclusion of the new turbulent term $T_{ijt} = -\overline{\rho u_i' u_j'}$, which represents nine additional turbulent shear stress components caused by the cross-products of the fluctuating velocity components and are referred to as the Reynolds stress components. The nine components Reynolds stress tensor can be summarized by the following:

$$T_{ij_t} = -\overline{\rho u_i' u_j'} = \rho \begin{vmatrix} \overline{u'^2} & \overline{u'v'} & \overline{u'w'} \\ \overline{u'v'} & \overline{v'^2} & \overline{v'w'} \\ \overline{u'w'} & \overline{v'w'} & \overline{w'^2} \end{vmatrix} \tag{8}$$

The total stress is written as the sum of laminar viscous shear and turbulent Reynolds stress as

$$T_{ij} = -\rho\overline{u_i' u_j'} + \mu\left(\frac{\partial u_i}{\partial x_j} + \frac{\partial u_j}{\partial x_i}\right) \tag{9}$$

The new nine-component turbulent stress tensor depend not only on the fluid properties but also on the flow conditions such as geometry, velocity surface roughness and the up stream conditions, and defined based on the turbulence structure, which needs to be defined as well. Major challenge is to express Reynolds stress tensor in terms mean flow. Two approaches to evaluate the Reynolds stresses in terms of mean flow variables are 1. Boussinesq Eddy viscosity concept and Pradndtl Mixing Length model and 2. Reynolds Stress Transport Model.

Boussinesq eddy viscosity concept and Prandtl mixing length model

In an effort to mathematically describe turbulent stress in terms of mean flow quantities, Boussinesq (1877) introduced the concept of *eddy viscosity* using the analogy with the Newtonian viscous linear stress and strain rate relationship. Boussinesq assumption relates Reynolds turbulent stresses to the mean flow and strain rate in similarity with laminar linear shear-stress – strain relation as follows:

$$\tau_t = -\rho\overline{u'v'} = \mu_t\left(\frac{du}{dy} + \frac{dv}{dx}\right) \tag{10}$$

Where μ_t is term as the turbulent viscosity or eddy viscosity and the total stress is given as

$$\tau_t = (\mu + \mu_t)\left(\frac{du}{dy} + \frac{dv}{dx}\right) \tag{11}$$

This leads to general expression for the Reynolds stress tensor expressed as

$$T_{ij_t} = \left[\mu_t\left(\frac{\partial u_i}{\partial x_j} + \frac{\partial u_j}{\partial x_i}\right)\right] - \frac{2}{3}\mu_t\frac{\partial u_k}{\partial x_k}\delta_{ij} \tag{12}$$

and the total stress is expressed as the sum of laminar and turbulent stress

$$T_{ij} = \left[\mu_{tot}\left(\frac{\partial u_i}{\partial x_j} + \frac{\partial u_j}{\partial x_i}\right)\right] - \frac{2}{3}\mu_{tot}\frac{\partial u_k}{\partial x_k}\delta_{ij} \tag{13}$$

Where $\mu_{tot} = \mu + \mu_t$ = total viscosity, which is the sum of the molecular dynamic viscosity, μ and turbulent or eddy viscosity, μ_t.

Turbulent or eddy viscosity value is generally several order of magnitude higher than the molecular dynamic viscosity depending on the order of magnitude of the turbulence in the flow Another important characteristic of turbulent or eddy viscosity is that it depends not only on the fluid, but it varies throughout the flow domain and depends strongly on fluid flow characteristics, geometry, roughness and upstream conditions. Prandtl in 1925 introduced the concept of mixing length (l_m) theory that closely relates to eddy viscosity

concept and form the basis for all turbulent modeling effort. The Prandtl mixing length is defined as the average distance travelled by a lump of fluid or the fluid eddy in the normal direction to the flow in similarity with the mean free path length of molecules. Based on this concept, the turbulent stress and turbulent eddy viscosity are expressed in terms of Prandtl mixing length as follows:

$$\tau_t = -\rho\overline{u'v'} = \rho l_m^2 \left(\frac{\partial u}{\partial y}\right)^2 \tag{14}$$

and

$$\mu_t = l_m^2 \left(\frac{\partial u}{\partial y}\right) \tag{15}$$

Different classes of turbulence closure models:

Turbulence closure models takes into account of statistical average effect of small scale eddies on the time averaged mean flow that only resolves large scale eddies. In order to define the turbulent eddy viscosity, it is necessary determine a suitable velocity scale and a length scale. The mixing length model is considered as an algebraic model or a zero-equation turbulence model. Subsequently additional class of turbulence models were developed based on number of additional equations to describe the turbulent viscosity. An **n**-equation turbulence model requires solution of **n** additional transport equations for additional variables used to describe the length and velocity scales used in the estimation of turbulent viscosity. In *one-equation* turbulence model, *turbulence kinetic energy* **(k)** was introduced to describe the velocity scale. Subsequently, in *two-equation model*, additional variable like the rate of dissipation of turbulence kinetic energy was introduced to represent the length scale of turbulence. The estimation of turbulence viscosity in terms of turbulence kinetic energy (k) and turbulence dissipation rate (ε) is given by the Prandtl-Kolmogorov relation:

$$\mu_t = \rho C_\mu k^2 / \varepsilon \tag{16}$$

Turbulence models are classified into following several divisions and subdivisions:

i. **Algebraic turbulence or Zero-equation model**
   Algebraic turbulence models are zero-equation turbulence models that do not require the solution of any additional equation, and are calculated directly from the flow variables. As a consequence, zero equation models do not take into account history effects of the turbulence, such as convection and diffusion of turbulent energy and are often adequate for simpler flow geometries. Some of the most popular algebraic zero-equation turbulence models are a) Cebeci-Smith model, b) Baldwin-Lomax model and c) Johnson-King model. Algebraic models are simple, quite robust and computationally less expensive. Major limitation of the algebraic turbulence are that they are semi-empirical with weak physical base and so not applicable to flow problems that are significantly different from flow problems for which the empirical constant are derived.
ii. **One-equation model**
   One equation turbulence models include i) Prandtl's one-equation model, ii) Baldwin-Barth model and iii) Spalart-Allmaras model

- Spalart – Allmaras model
  The model proposed by Spalart and Allmaras is a one-equation model that solves for kinematic eddy viscosity from the transport equation. It is the preferred model for problems involving no separation or weak separation and it is widely used in turbomachinary applications. The transport equation is given by

$$\frac{\partial}{\partial t}(\rho\tilde{\nu})+\frac{\partial}{\partial x_i}(\rho\tilde{\nu}u_i)=G_\nu+\frac{1}{\sigma_{\tilde{\nu}}}[\frac{\partial}{\partial x_j}\{\mu+\rho\tilde{\nu})\frac{\partial\tilde{\nu}}{\partial x_j}\}+C_{b2}\rho(\frac{\partial\tilde{\nu}}{\partial x_j})^2]-Y_{\tilde{\nu}} \tag{17}$$

Where G is the production of turbulent viscosity and $Y_{\tilde{\nu}}$ is the destruction of turbulent viscosity that occurs in the near-wall region. The turbulent viscosity (μ_t) is computed as

$$\mu_t=\rho\tilde{\nu}f_{\nu1} \tag{18a}$$

Where $f_{\nu1}$ is the viscous damping function given by

$$f_{\nu1}=\frac{\chi^3}{\chi^3+C_{\nu1}^3},\chi=\frac{\tilde{\nu}}{\nu} \tag{18b}$$

$$G_\nu=C_{b1}\rho\tilde{S}\tilde{\nu} \tag{18c}$$

$\tilde{S}$ is a function of mean rate of rotation tensor and viscous damping function.

$$Y_{\tilde{\nu}}=C_{w1}\rho f_w(\frac{\tilde{\nu}}{d})^2 \tag{18d}$$

Where f_{w1} is a function of vorticity and d is the distance from the wall.

iii. Two-equation model

Two equation turbulence models include two extra transport equations to represent the turbulent properties of the flow that accounts for convection and diffusion of turbulent energy. Most often one of the transported variables is the **turbulent kinetic energy**, k. The second transport variables varies, however, with different two-equation models. Most common choices are the **turbulent dissipation**, ε, or the **specific dissipation**, ω. While the **turbulent kinetic energy**, k represents the energy in the turbulence, the **turbulent dissipation**, ε, or the **specific dissipation**, ω represents the turbulence length-scale. A list of some of these widely used two-equation turbulence models is given here:

$k-\varepsilon$ **Turbulence models:** $k-\varepsilon$ High Reynolds turbulence model, $k-\varepsilon$ Low Reynolds turbulence model, Realisable $k-\varepsilon$ model, $k-\varepsilon$ Renormalization Group (RNG) turbulence model, $k-\varepsilon$ Chen turbulence model, $k-\varepsilon$ Standard Quadratic High Reynolds Turbulence model, $k-\varepsilon$ Suga Quadratic High Reynolds Turbulence models

$k-\omega$ **Turbulence models:** $k-\omega$ Standard High Re, $k-\omega$ Standard Low Re, $k-\omega$ SST High Re and $k-\omega$ SST Low Re

iv. Reynolds Stress Model (RSM)

Reynolds stress model (RSM) discarded the eddy viscosity approach and computes the Reynolds stresses directly. It is a higher level more elaborate turbulent model, which

introduces exact Reynolds stress transport equations to compute the Reynolds stresses directly and accounts for the directional effects of Reynolds stress field. Some of the most popular RSM model are RSM/Gibson-Launder (wall Reflection: Standard), RSM/Gibson-Launder (wall Reflection: Craft) and RSM/Speziale, Sarkar and Gatski.

2.2.3 The Standard κ - ε model

The standard $k-\varepsilon$ turbulence model is the most widely used one, which is also known as $k-\varepsilon$ High Reynolds turbulence model. It includes two transport equations to define the turbulence scales. The k denotes the turbulent kinetic energy (m^2/s^2), whereas ε denotes the dissipation rate (m^2/s^3). The model proposed by Launder and Spalding [1974] is based on the transport equations for the turbulent kinetic energy, k and its rate of dissipation, ε as follows.

$$\frac{\partial}{\partial t}(\rho k)+\frac{\partial}{\partial x_i}(\rho k u_i)=\frac{\partial}{\partial x_j}\left[\left(\mu+\frac{\mu_t}{\sigma_k}\right)\frac{\partial k}{\partial x_j}\right]+G_b-\rho\varepsilon-Y_M+S_k \tag{19}$$

$$\frac{\partial}{\partial t}(\rho\varepsilon)+\frac{\partial}{\partial x_i}(\rho\varepsilon u_i)=\frac{\partial}{\partial x_j}\left[\left(\mu+\frac{\mu_t}{\sigma_\varepsilon}\right)\frac{\partial \varepsilon}{\partial x_j}\right]+C_{1\varepsilon}\frac{\varepsilon}{k}(C_{3\varepsilon}G_b)-C_{2\varepsilon}\rho\frac{\varepsilon^2}{k}+S_\varepsilon \tag{20}$$

The generation of turbulent kinetic energy due to buoyancy is

$$G_b=-g_i\frac{\mu_t}{\rho\,\mathrm{Pr}_t}\frac{\partial\rho}{\partial x_i} \tag{21}$$

The fluctuating dilatation in compressible turbulence to the overall dissipation rate

$$Y_M=\frac{2\rho\varepsilon\kappa}{a^2} \tag{22}$$

Where, a = Speed of sound.

The turbulent viscosity is computed by combining k and ε as

$$\mu_t=\rho C_\mu\frac{k^2}{\varepsilon} \tag{23}$$

Where, $C_\mu=0.09$, $C_{1\varepsilon}=1.44$, $C_{2\varepsilon}=1.92$ and, $C_{3\varepsilon}=0.09$ are model constants. $\sigma_k=1.0$ and $\sigma_\varepsilon=1.3$ are the turbulent Prandtl numbers for k and ε respectively. S_κ and S_ε are user-defined source terms.

A two-equation $k-\varepsilon$ model could be quite suitable for flow in straight channels without the presence of any large scale flow separations and adverse pressure gradient or in problems where only average parameters are to be determined without the requirement of resolving detail turbulence quantities. This model is found to be quite adequate for many industrial applications.

2.2.4 Low Reynolds k - ε turbulence model

The failure of standard $k-\varepsilon$ model to predict the low-Re and separated flows, introduces the $k-\varepsilon$ Low-Re turbulence model {Lam and Bremhorst (1981), Jones and Launder (1972)

and Majumdar and Deb (2003)], which has a special near-wall treatment for proper prediction of the flow at a region very near to the wall, referred to as the laminar sub-layer. It is well known that the turbulent kinetic energy distribution reaches to its peak value in the near-wall region. Though ε increases in this region, k also increase and k^2 plays a very important role by changing the μ_t by a large extent. On the other hand, at a location very close to the wall, k^2 suppresses μ_t. To counteract these effects, two approaches have been taken:

a. The wall-function method, where an empirical wall function has been introduced along with k and ε equations. However, it is not suitable for many flows.
b. The low-Reynolds-number method, where the wall boundary conditions are directly applied to the equations without introducing any wall functions.

Jones and Launder [11] extended the standard k-ε model to the low Reynolds number model, which allows calculation through the viscous sub-layer to the wall without using wall function formulas. Additional terms were included in the equations for dissipation rate. The equations for the rate of dissipation and the turbulence kinetic energy included viscous diffusion term to ensure that the total dissipation rate is non-zero at the wall and modified terms containing C's to make them dependent upon Reynolds number of turbulence. The k equation for this TM is the same as equation (19), except the expression of the term μ_t, which is defined as

$$\mu_t = f_\mu \frac{C_\mu \rho . k^2}{\varepsilon} \tag{24}$$

where

$$f_\mu = \left[1 - e - 0.0198 \mathrm{Re}_y\right]\left[1 + \frac{5.29}{\mathrm{Re}_y}\right] \tag{25}$$

ε equation:

$$\frac{\partial}{\partial t}(\rho\varepsilon) + \frac{\partial}{\partial x_j}\left[\rho u_j \varepsilon - \left(\mu + \frac{\mu_t}{\sigma_\varepsilon}\right)\frac{\partial \varepsilon}{\partial x_j}\right] = C_{\varepsilon 1}\frac{\varepsilon}{k}\left\{\mu_t\left(P + P_{NL} + P'\right) - \frac{2}{3}\left(\mu_t \frac{\partial u_i}{\partial x_j} + \rho k\right)\frac{\partial u_i}{\partial x_j}\right\} + C_{\varepsilon 3}\frac{\varepsilon}{k}\mu_t P_B - C_{\varepsilon_2}\left(1 - 0.3e^{-R_t^2}\right)\rho\frac{\varepsilon^2}{k} + C_{\varepsilon_4}\rho\varepsilon\frac{\partial u_i}{\partial x_j} \tag{26}$$

The additional term P' is given by

$$P' = 1.33\left(1 - 0.3e^{-R_t^2}\right)\left[P + P_{NL} + 2\frac{\mu}{\mu_t}\frac{k}{y^2}\right]e^{-0.00375\,\mathrm{Re}_y^2} \tag{27}$$

Where $\mathrm{Re}_y = \frac{y\sqrt{k}}{v}$, y = a normal distance to the nearest wall and $R_t = \frac{k^2}{v\varepsilon}$ = Turbulent Reynolds Number.

2.2.5 k - ε Chen turbulence model

The Chen model has been introduced to have a better response of the energy transfer mechanism of turbulence towards the mean strain rate. It does not take into account of the compressibility and buoyancy effects explicitly.

Equation for k :

$$\frac{\partial}{\partial t}(\rho k)+\frac{\partial}{\partial x_j}\left[\rho u_j k-\left(\mu+\frac{\mu_t}{\sigma_k}\right)\frac{\partial k}{\partial x_j}\right]=\mu_t(P+P_B)-\rho\varepsilon-\frac{2}{3}\left(\mu_t\frac{\partial u_i}{\partial x_j}+\rho k\right)\frac{\partial u_i}{\partial x_j} \tag{28}$$

Equation for ε :

$$\begin{aligned}&\frac{\partial}{\partial t}(\rho\varepsilon)+\frac{\partial}{\partial x_j}\left[\rho u_j\varepsilon-\left(\mu+\frac{\mu_t}{\sigma_\varepsilon}\right)\frac{\partial\varepsilon}{\partial x_j}\right]=C_{\varepsilon1}\frac{\varepsilon}{k}\left[\mu_t P-\frac{2}{3}\left(\mu_t\frac{\partial u_i}{\partial x_j}+\rho k\right)\frac{\partial u_i}{\partial x_j}\right]+\\&+C_{\varepsilon3}\frac{\varepsilon}{k}\mu_t P_B-C_{\varepsilon2}\rho\frac{\varepsilon^2}{k}+C_{\varepsilon4}\rho\varepsilon\frac{\partial u_i}{\partial x_j}+C_{\varepsilon5}\frac{\mu^2{}_t}{\rho}\frac{P^2}{k}\end{aligned} \tag{29}$$

2.2.6 Suga's High Reynolds number $k-\varepsilon$ turbulence model:

In Suga's $k-\varepsilon$ model $\tilde{\varepsilon}$ is solved instead of ε, which is the isotropic part of ε and is zero at the wall. The k equation for this TM is same as equation (19) and the dissipation equation is given as

Equation for ε :

$$\frac{\partial}{\partial t}(\rho\tilde{\varepsilon})+\frac{\partial}{\partial x_j}\left[\rho u_j\tilde{\varepsilon}-\left(\mu+\frac{\mu_t}{\sigma_\varepsilon}\right)\frac{\partial\tilde{\varepsilon}}{\partial x_j}\right]=\rho C_{\varepsilon1}\frac{\tilde{\varepsilon}}{k}P_k-\rho C_{\varepsilon2}+C_{\varepsilon3}\frac{\tilde{\varepsilon}}{k}\mu_t P_B+C_{\varepsilon4}\rho\tilde{\varepsilon}\frac{\partial u_i}{\partial x_i} \tag{30}$$

Where

$$P_B\equiv\frac{g_i}{\sigma_{h,t}}\frac{1}{\rho}\frac{\partial\rho}{\partial x_j},\quad P_k=-\overline{u_i'u_j'}\frac{\partial u_i}{\partial x_j},\quad \tilde{R}_t=\frac{k^2}{v\tilde{\varepsilon}},\quad \tilde{\varepsilon}=\varepsilon-2\nu\left[\frac{\partial\sqrt{k}}{\partial x_i}\right]^2$$

Turbulent viscosity μ_t is defined as

does not take into account of $$\mu_t=f_\mu\frac{C_\mu\rho.k^2}{\varepsilon} \tag{31}$$

Where

$$f_\mu=1-\exp\left[-\left(\frac{\tilde{R}_t}{90}\right)^{\frac{1}{2}}-\left(\frac{\tilde{R}_t}{400}\right)^2\right] \tag{32}$$

2.2.7 The Renormalization Group (RNG) $\kappa-\varepsilon$ model

The renormalization group (RNG) κ-ε model [Choudhury, D. (1993)] originated from the instantaneous Navier-Stokes equations, utilizing a mathematical technique called renormalization group (RNG) method. This derivation results in additional terms and functions in transport equations of k and ε .

Transport equation for the RNG $\kappa-\varepsilon$ model

The RNG $\kappa-\varepsilon$ model has similar form to the standard $\kappa-\varepsilon$ model:

$$\frac{\partial}{\partial t}(\rho k)+\frac{\partial}{\partial x_i}(\rho k u_i)=\frac{\partial}{\partial x_i}(\sigma_k u_{eff}\frac{\partial k}{\partial x_j})+G_b-\rho\varepsilon-Y_M+S_K \tag{33}$$

$$\frac{\partial}{\partial t}(\rho\varepsilon)+\frac{\partial}{\partial x_i}(\rho\varepsilon u_i)=\frac{\partial}{\partial x_i}(\sigma_\varepsilon u_{eff}\frac{\partial \varepsilon}{\partial x_j})+C_{1\varepsilon}C_{3\varepsilon}G_b-C_{2\varepsilon}\rho\frac{\varepsilon^2}{k}-R_\varepsilon+S_\varepsilon \tag{34}$$

The RNG theory results in a differential equation for *turbulent viscosity:*

$$d\left(\frac{\rho^2 k}{\sqrt{\varepsilon\mu}}\right)=1.72\frac{\hat{v}}{\sqrt{\hat{v}^3-1+C_v}}d\hat{v} \tag{35}$$

Where $\hat{v}=\frac{\mu_{eff}}{\mu}$ and $C_v\approx 100$

Turbulent quantities change considerably with the effect of swirl in the mean flow direction. To incorporate the swirl effect the turbulent viscosity is calculated form

$$\mu_t=\mu_{t0}f\left(\alpha_s,\Omega,\frac{\kappa}{\varepsilon}\right) \tag{36}$$

Where μ_{t0}, is the turbulent viscosity calculated without swirl modification from equation (35), α_s = 0.05, for moderately swirl flow, Ω swirl number. For higher Reynolds numbers equation turbulent viscosity is calculated by equation (16) and c_μ = 0.0845. The default model constants are $C_{1\varepsilon}=1.42$, $C_{2\varepsilon}=1.68$.

2.2.8 The Realizable $\kappa-\varepsilon$ model

The Realizable $\kappa-\varepsilon$ model [Shih, T. and Liou, W. (1995)] includes additional mathematical constraints consistent with certain physics of the turbulent flow. It addresses the deficiencies of traditional $\kappa-\varepsilon$ models by adopting a new eddy-viscosity formula with a variable Cμ and a new model equation for dissipation rate ε based on dynamic equations mean-square vorticity fluctuation. The transport equations in realizable $\kappa-\varepsilon$ model are

$$\frac{\partial}{\partial t}(\rho k)+\frac{\partial}{\partial x_i}(\rho k u_j)=\frac{\partial}{\partial x_i}\left[\left(\mu+\frac{\mu_t}{\sigma_k}\right)\frac{\partial k}{\partial x_j}\right]+G_b-\rho\varepsilon-Y_M+S_k \tag{37}$$

$$\frac{\partial}{\partial t}(\rho\varepsilon)+\frac{\partial}{\partial x_j}(\rho\varepsilon u_j)=\frac{\partial}{\partial x_i}\left[\left(\mu+\frac{\mu_t}{\sigma_\varepsilon}\right)\frac{\partial \varepsilon}{\partial x_j}\right]+\rho C_1 S\varepsilon-\rho C_2\frac{\varepsilon^2}{\kappa+\sqrt{\nu\varepsilon}}+C_{1\varepsilon}\frac{\varepsilon}{k}C_{3\varepsilon}G_b+S_k \tag{38}$$

Where $C_1=\max\left[0.43,\frac{\eta}{\eta+5}\right]$, $\eta=S\frac{k}{\varepsilon}$, $C_{1\varepsilon}$ =1.44, C_2 =1.9, σ_k =1.0 and σ_ε =1.2 are the model constants. The eddy viscosity is calculated from equation (16), but

$$C_\mu = \frac{1}{A_0 + A_s \frac{kU^*}{\varepsilon}} \tag{39}$$

$$U^* \equiv \sqrt{S_{ij}S_{ij} + \tilde{\Omega}_{ij}\tilde{\Omega}_{ij}} \tag{40}$$

Where $\tilde{\Omega}_{ij}$, is the mean rate-of-rotation tensor viewed in the rotating reference frame with an angular velocity. Both the Realizable and RNG k-ε models have shown substantial improvements over the standard k-ε model where the flow features include strong streamline curvature, vortices, and rotation.

The realizable κ-ε model provides superior performance for flows involving rotation, boundary layers under strong adverse pressure gradients, separation, and recirculation. The limitations of the realizable κ-ε model are that it produces nonphysical turbulent viscosities in situations when the computational domain contains both rotating and stationary fluid zones, i.e., use of multiple reference frames or rotating sliding meshes.

2.2.9 Quadratic High Reynolds *k-ε* turbulence model

Non-linear turbulence models are introduced to take into account of anisotropic turbulence characteristics present in many real flows by adopting non-linear relationships between Reynolds stresses and the rate of strain. For quadratic models, the constitutive relations for the Reynolds stresses are:

$$\rho\frac{\overline{u_i'u_j'}}{k} = \frac{2}{3}\left(\frac{\mu_t}{k}\frac{\partial u_k}{\partial x_k} + \rho\right)\delta_{ij} - \frac{\mu_t}{k}S_{ij} + C_1\frac{\mu_t}{\varepsilon}\left[S_{ik}S_{kj} - \frac{1}{3}\delta_{ij}S_{kl}S_{kl}\right] + C_2\frac{\mu_t}{\varepsilon}\left[\Omega_{ik}S_{kj} + \Omega_{jk}S_{ki}\right] + C_3\frac{\mu_t}{\varepsilon}\left[\Omega_{ik}\Omega_{ik} - \frac{1}{3}\delta_{ij}\Omega_{kl}\Omega_{kl}\right] \tag{41}$$

Where, Ω_{ij} is the mean vorticity tensor given by

$$\Omega_{ij} = \frac{\partial u_i}{\partial x_j} - \frac{\partial u_j}{\partial x_i} \tag{42}$$

Coefficients are defined as,

$$C_1 = \frac{c_{NL1}}{\left(c_{NL6} + c_{NL7}S^3\right)C_\mu}, \quad C_2 = \frac{c_{NL2}}{\left(c_{NL6} + c_{NL7}S^3\right)C_\mu}, \quad C_3 = \frac{c_{NL3}}{\left(c_{NL6} + c_{NL7}S^3\right)C_\mu} \tag{43}$$

Where,

$C_\mu = \frac{c_{A0}}{c_{A1} + c_{A2}S + c_{A3}\Omega}$, $S = \frac{k}{\varepsilon}S^*$ and $\Omega = \frac{k}{\varepsilon}\Omega^*$,

$S^* = \sqrt{\frac{1}{2}S_{ij}S_{ij}}$ and $\Omega^* = \sqrt{\frac{1}{2}\Omega_{ij}\Omega_{ij}}$

c_{A0}	c_{A1}	c_{A2}	c_{A3}	c_{NL1}	c_{NL2}	c_{NL3}	c_{NL6}	c_{NL7}
0.667	1.25	1.0	0.9	0.75	3.75	4.75	1000.0	1.0

Table 1. Empirical coefficients for $k-\varepsilon$ quadratic high Re turbulence model

2.2.10 $k-\omega$ SST (Shear Stress Transport Turbulence) model

An alternate approach to the $k-\varepsilon$ model is the $k-\omega$ model, where ω is the specific dissipation rate, which is defined as

$$\omega = \varepsilon / C_{\mu}\, k \tag{44}$$

Equation for k:

$$\frac{\partial}{\partial t}(\rho k)+\frac{\partial}{\partial x_j}\left[\rho u_j k-\left(\mu+\frac{\mu_t}{\sigma_k^{\omega}}\right)\frac{\partial k}{\partial x_j}\right]=\mu_t\left(P+P_B\right)-\rho\beta^* k\omega \tag{45a}$$

Equation for ω:

$$\frac{\partial}{\partial t}(\rho\omega)+\frac{\partial}{\partial x_j}\left[\rho u_j\omega-\left(\mu+\frac{\mu_t}{\sigma_{\omega}^{\omega}}\right)\frac{\partial\omega}{\partial x_j}\right]=\alpha\frac{\omega}{k}\mu_t P-\rho\beta\omega^2+\rho S_{\omega}+C_{\varepsilon 3}\mu_t P_B C_{\mu}\omega \tag{45b}$$

Where, C_{μ} and $C_{\varepsilon 3}$ are empirical coefficients.

The coefficients are expressed as follows:

$$C_{\phi}=F_1 C_{\phi 1}+(1-F_1)C_{\phi 2}$$

Where $C_{\phi 1}$ and $C_{\phi 2}$ are given by two separate coefficient sets and

$$F_1=\tanh\left(arg_1^4\right)$$

$$arg_1=\min\left[\max\left(\frac{\sqrt{k}}{0.09\omega y},\frac{500\nu}{y^2\omega}\right),\frac{4\rho k}{\sigma_{\omega 2}^{\omega}CD_{k\omega}y^2}\right]$$

$$CD_{k\omega}=\max\left(\frac{2\rho}{\omega\sigma_{\omega 2}^{\omega}}\frac{\partial k}{\partial x_j}\frac{\partial\omega}{\partial x_j},10^{-20}\right)$$

Where

σ_{k1}^{ω}	$\sigma_{\omega 1}^{\omega}$	β_1	β_1^*	κ
1.176	2.0	0.075	0.09	0.41

Table 2. Coefficients for $k-\omega$ SST turbulence model

With,

$$\alpha_1=\frac{\beta_1}{\beta_1^*}-\frac{\kappa^2}{\sigma_{\omega 1}^{\omega}\sqrt{\beta_1^*}}$$

σ_{k2}^{ω}	$\sigma_{\omega 2}^{\omega}$	β_2	β_2^*	κ
1.0	1.168	0.0828	0.09	0.41

Table 3. Coefficients for $k-\omega$ SST turbulence model

With,

$$\alpha_2 = \frac{\beta_2}{\beta_2^*} - \frac{\kappa^2}{\sigma_{\omega 2}^{\omega}\sqrt{\beta_2^*}}, \qquad S_{\omega} = 2(1-F_1)\frac{1}{\sigma_{\omega 2}^{\omega}\omega}\frac{\partial k}{\partial x_j}\frac{\partial \omega}{\partial x_j}$$

The *turbulent viscosity* is defined as,

$$\mu_t = \rho\frac{a_1 k}{max\left(a_1\omega, \Omega^* F_2\right)}$$

Where,

$a_1 = 0.31$, $F_2 = tanh\left(arg_2^2\right)$

and

$$arg_2 = max\left(2\frac{\sqrt{k}}{0.09\omega y}, \frac{500\nu}{y^2\omega}\right)$$

Like standard $k-\varepsilon$ model, the $k-\omega$ model is also widely used in many industrial applications involving flow separation and recirculation.

2.2.11 Reynolds Stress Model

In the Reynolds stress model [Gibson and Launder (1978), Launder (1989) and Launder et al. (1975)], additional transport equations are used in the calculation of the Reynolds stresses. The stresses obtained are used to calculate the average momentum. Due the additional transportation equations, Reynolds stress model (RSM) model shows superior results with flows involving anisotropic turbulence. It includes seven additional equations and account for higher accuracy and however, require additional computational resources.

$$\frac{\partial}{\partial t}(\rho u_i) + \frac{\partial}{\partial x_j}\left(\rho u_i u_j\right) = \frac{\partial p}{\partial x_i} + \frac{\partial}{\partial x_j}\left[\mu\left(\frac{\partial u_i}{\partial x_j} + \frac{\partial u_j}{\partial x_i} - \frac{2}{3}\delta_{ij}\frac{\partial u_l}{\partial x_l}\right)\right] + \frac{\partial}{\partial x_j}\left(-\rho\,\overline{u_i' u_j'}\right) \tag{46a}$$

$$\frac{\partial}{\partial t}\left(\rho\,\overline{u_i' u_j'}\right) + \frac{\partial}{\partial x_k}\left(\rho u_k\,\overline{u_i' u_j'}\right) = \frac{\partial}{\partial x_k}\left[\rho\,\overline{u_i' u_j' u_k'} + p\left(\delta_{kj}\overline{u_i'} + \delta_{ik}\overline{u_j'}\right)\right]$$
$$+ \frac{\partial}{\partial x_k}\left[\mu\frac{\partial}{\partial x_k}\left(\overline{u_i' u_j'}\right)\right] - \rho\left(\overline{u_i' u_k'}\frac{\partial u_j}{\partial x_k} + \overline{u_j' u_k'}\frac{\partial u_i}{\partial x_k}\right) - \rho\beta\left(g_i\,\overline{u_j'\theta} + g_i\,\overline{u_j'\theta}\right)$$
$$+ p\left(\frac{\partial \overline{u_i'}}{\partial x_j} + \frac{\partial \overline{u_i'}}{\partial x_j}\right) - 2\mu\frac{\partial \overline{u_i'}}{\partial x_k}\frac{\partial \overline{u_j'}}{\partial x_k} - 2\rho\Omega_k\left(\overline{u_j' u_m'}\varepsilon_{ikm} + \overline{u_i' u_m'}\varepsilon_{jkm}\right) \tag{46b}$$

Like any other transport equation the Equation (46b) for the Reynolds stress transport includes number of terms including convection, turbulent diffusion, molecular diffusion, buoyancy, stress production, and rotation production, pressure strain, viscous dissipation and user defined source term. Some of the most commonly used RSM models are i. Gibson and Launder model and ii) Speziale, Sarker and Gatski model.
A RSM model is generally required in problems involving strong anisotropic effects.
Usually one would start with the simplest model such as the standard model with wall function or a low Reynolds number model with fine mesh size near the wall to see if reasonably acceptable engineering results are obtained. In order to narrow down the choice of turbulence model in terms of stable converging solutions, each class of turbulence models are to compared among themselves first before comparing all models with the experimental data or DNS/LES.

2.3 Boundary condition for turbulence quantities

One of major requirement for the solution of turbulent flow is the specification of turbulence quantities such as turbulence kinetic energy and turbulence dissipation rate or the mixing length or the ratio of turbulence viscosity to molecular viscosity at the inlet. While results are not strongly influenced by the inlet turbulence level for problems with inlet located far away from the region of interest, the specified values have a significant effect on the resulting flow solution for problems with smaller entry length. So, one approach is to assign directly the values of turbulent kinetic energy and turbulent dissipation rate. However, specification of turbulence quantities such as turbulence kinetic energy and turbulence dissipation rate at inlet can be quite difficult and often rely on engineering judgments. It is always, however, preferred to assign experimentally measured values of turbulence quantities. If such data are not available, then values can be prescribed based on engineering assumptions and a numerical sensitivity study must be performed to understand the sensitivity of inlet turbulence conditions on the solutions.
For the specification of the turbulent kinetic energy, appropriate values can be specified through *turbulence intensity* (I), which is defined by the ratio of the fluctuating components of the velocity to the mean velocity. In general, the inlet turbulence is a function of the upstream flow conditions. Approximate values for the turbulence kinetic energy can be determined according to the following relationship:

$$k_{inlet} = \frac{3}{2}\left(U_{inlet} I\right)^2 \tag{47a}$$

Inlet dissipation rate can be specified based length scale as

$$\varepsilon_{\text{inlet}} = \frac{C_{\mu}^{3/4} k^{3/2}}{l} \tag{47b}$$

Where $l = 0.1 D_H$
In external aerodynamic flows over airfoils, the turbulence intensity level is typically 0.3%
For atmospheric boundary layer flows, the level can be as high as two orders of magnitude – 30%. The range of turbulence intensity for a moderately turbulent flow is around 1-10%.

The turbulence intensity at the core of a fully developed duct flow is estimated from the following formula:

$$I = 0.16\left(\mathrm{Re}_{DH}\right)^{1/8} \tag{48}$$

Near-wall region modeling

Another important aspect of using some of the turbulence closure models are that they are valid only in the fully turbulent region due to the laminarization of flow or the presence of laminar viscous sub-layer near the wall. In regions close to the wall, viscous effects dominate over turbulence effects due to the small local Reynolds number of turbulence. The near-wall modeling consists of two approaches. The *first approach* involves modifying the turbulence models such as low Reynolds number models and by using an appropriate fine grid to resolve the near-wall viscous effects. In low Reynolds number modeling methods k and ε equations are modified such that they are valid throughout the laminar, semi-laminar and fully turbulent regions

In the *second approach,* the viscosity-affected region is not resolved and *wall functions* are used to bridge the viscosity-affected region between the wall and the fully turbulent region. The standard high Reynolds number turbulence models need not be modified if the wall functions are used to account for the presence of walls. The two most popular types of wall functions are the standard wall functions and non-equilibrium wall functions.

In the wall function method the grid size distribution is selected in such a way that the adjacent grid point P is sufficiently remote from the wall. This causes local Reynolds number of turbulence at point P to be much greater than one, so that the viscous effects are dominating in this region. The standard wall functions proposed by Launder and Spalding [17] relate the non-dimensional distance (y^+) to the distance of the nearest cell point P (y_p) from the wall as

$$y^+ = \frac{\rho C_\mu^{1/4} k_P^{1/2} y_P}{\mu}$$

Where k_p is the turbulent kinetic energy at point P and μ is the dynamic viscosity of the fluid.

In addition, the momentum and heat flux between the wall and the adjacent grid point P is assumed to obey certain relations in the numerical calculations. The refined mesh size distribution near the wall is limited by satisfying y^+ requirement, which defines the minimum distance of the computational cell from the wall boundary. Having the correct y^+ value for the cells next to the wall is extremely important to obtain the correct velocity, pressure and shear stress values. Also for using turbulence models with wall functions, the y^+ value of the near wall cells is a basic requirement that has to be satisfied. All computational turbulence studies starts with an initial search for the correct cell size to satisfy the y^+ requirement for the turbulence model used. For example, in the study of $k-\varepsilon$ high Reynolds number turbulence closure model with standard wall function the y^+ value are required to be kept within 30 – 120.

Non-equilibrium wall functions solve for mean velocity near the wall region incorporating pressure gradient effects. The non-equilibrium wall function employs a two-layer concept in computing the turbulence kinetic energy at the wall-adjacent cells. The standard wall

functions are generally used for high Reynolds number wall bounded flows and for satisfying equilibrium conditions for production and dissipation of turbulent kinetic energy at the wall. For flows that involve adverse pressure gradient, rotation, and strong streamline curvature, the flow conditions depart from equilibrium. The non-equilibrium wall functions take into account of the effects of pressure gradient and departure from equilibrium conditions and are generally involve severe pressure gradient.

3. Case study examples

3.1 Case – I: Computational fluid dynamic analysis of turbulent flow in blade passages of centrifugal fan impeller

The objective of the present study is to analyze the three-dimensional turbulent flow in a single blade passage of a centrifugal fan impeller at design and off-design conditions. Numerical calculations are performed using commercial code FLUENT. A computational treatment of turbulent flow in a single blade passage of the centrifugal fan impeller is considered in this study. The geometric description of the impeller used for CFD simulation is presented in form of Pro/E solid model with different views describing the centrifugal fan geometrical features is shown in Figure 1. The assembly consists of a hub mounted on a back plate. The back plate is flat and circular with blades arranged in circular symmetry. The shroud is tapered from inlet to outlet with higher cross-sectional area at the inlet. The blades are straight and radial and their sectional width extends from the back plate all the way to the shroud, thus making the size of the tip gap region reduce to zero.

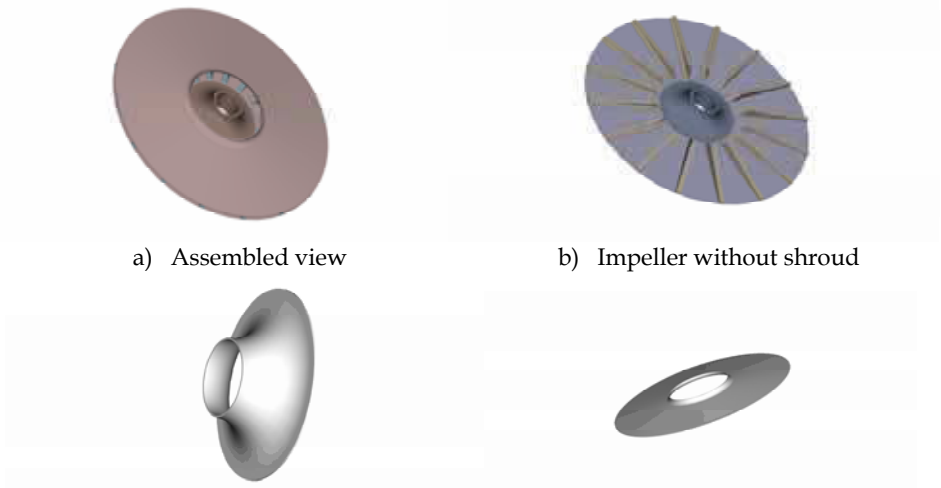

a) Assembled view b) Impeller without shroud

c) Impeller Hub d) Impeller shroud

Fig. 1. Solid model of the impeller design

3.1.1 Physical representation of the problem

A three-dimensional flow in a single blade passage of the centrifugal fan impeller is considered, taking into account of the cyclic nature of the flow and impeller geometry. The computational domain is depicted in Figure 2. Periodic boundaries are assumed at the inlet,

blade surface, and outlet. The flow includes important features like: Flow separation at the blade leading edge and Secondary flows arising in the channel due to centrifugal forces and Coriolis forces acting on the working fluid.

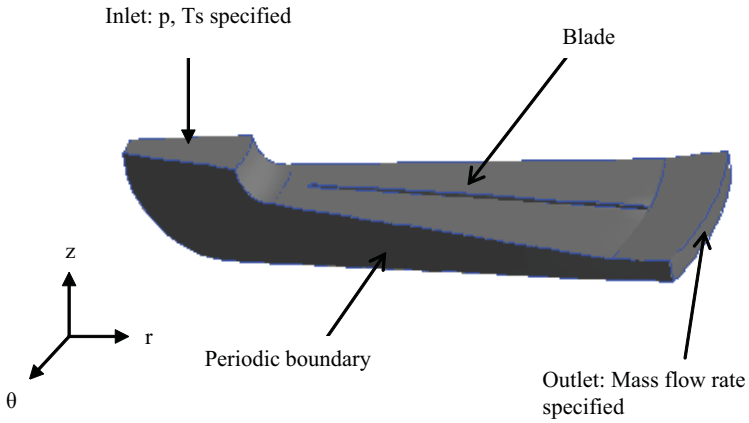

Fig. 2. Computational domain

A mathematical model for the flow field with associated boundary conditions and turbulence models are discussed

3.1.2 Governing equations

The RANS model for steady-state, turbulent, compressible flow in a rotating frame expressed in cylindrical coordinate system has been considered. Due to the rotation effects, the centrifugal forces and Coriolis forces act on the fluid. These effects are incorporated in the relative velocity formulation of the governing equations. The Reynolds turbulent stresses which arise due to the fluctuating velocity components are related to the mean flow variables calculated through different turbulence models. Turbulence closure model considered are 1. Spalart – Allmaras Model, 2. The Standard $\kappa-\varepsilon$ Model, 3. *The Realizable* $\kappa-\varepsilon$ *Model and 3. The RNG* $\kappa-\varepsilon$ *Model* The near-wall modeling is performed considering both the standard wall function and the non-equilibrium wall function. After initial evaluation of all turbulence models using both the wall functions, final results in the present study are presented with the standard wall functions in the RNG and standard κ-ε models, and the non-equilibrium wall functions are used for the realizable κ-ε model.

3.1.2.1 Boundary conditions

Inlet: Static pressure is specified at the channel inlet.
Outlet boundary condition: The mass flow outlet adjusts the exit pressure such that a target mass flow rate (i.e., mass flow at the inlet) is obtained at convergence. This type of approach is used in problems where the outlet static pressure is unknown at the beginning of solution.
Turbulence: The turbulent intensity and hydraulic diameter were specified at the inlet. The turbulent intensity is calculated based on Eq. (48).
Periodic boundary conditions are imposed between the channel inlet and outlet as the flow field is symmetric from blade to blade and the boundary conditions are uniform in circumferential direction. In the periodic boundary condition, each surface of the periodic

pair is treated as an internal surface. The pressure jump across the periodic boundaries was specified to be zero.

3.1.2.2 Flow Parameters

Reynolds number

The incoming flow into the impeller is from a circular pipe. Therefore the Reynolds number at the channel inlet is defined by

$$\mathrm{Re}_{in} = \frac{\rho v D}{\mu} \tag{48}$$

Where v is the velocity of the fluid, D is the hydraulic diameter
The Reynolds number at the channel exit is defined as

$$\mathrm{Re} = \frac{\rho C v_{\theta}}{\mu} \tag{49}$$

Where C is the chord length of the blade and V_θ is the tip speed of the impeller. For the base case (ω = 3300 RPM), the Reynolds number typically varies from 301900 to 1760000.

3.1.3 Computational model

A computational model based on the mathematical model presented is developed in GAMBIT. The edge set required to form the turbo volume was imported from Pro/E assembly file with edge set consisting of the hub, blade, and the casing cross-sections. Only a single blade passage was modeled assuming 22.5-degree (2*pi/Z) as the rotationally periodic conditions, Since there is no relative velocity difference between the fluid zone and the different wall zones (hub, blade, shroud), the whole geometry was modeled as a single rotating reference frame with the axis of rotation directed along the z-axis. After constructing the turbo volume, H template decomposition is adopted to split the volume bounded by the hub and casing with the surfaces representing the pressure and suction sides of the blades, and this results in four volumes as shown in Figure 3.

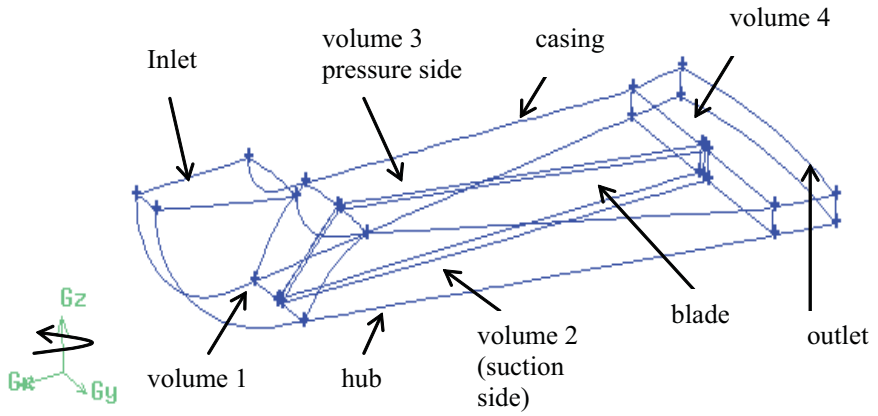

Fig. 3. Domain decomposition of turbo volume

3.1.3.1 Meshing the geometry

The mesh for the prescribed control volume shape and regulated order of spacing is achieved through a mapped meshing and using a combination of 8-node hexagonal brick volumes and 10-node clipped cube volumes. A soft nonuniform grading scheme is used for edge meshing. The turbo decomposition divides the impeller region into four volumes, each of which could be mapped with hexahedral structured mesh. It sets the interval count and grading on the edges and also sets face vertex types for the volume to be meshed. Hexahedral elements developed in the streamline direction of expected flow helps in improving the convergence of solution. The mesh for single blade passage grid is shown in Figure 4.

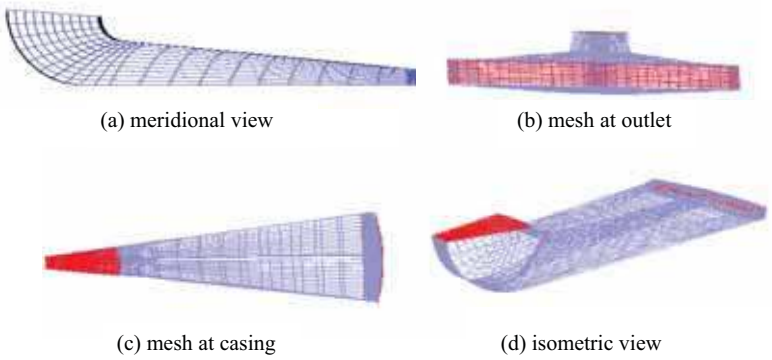

(a) meridional view (b) mesh at outlet

(c) mesh at casing (d) isometric view

Fig. 4. Single passage grid modeling

The grid system for the bases case consists of 78x40x30 hexahedral elements in pitch, axial and radial directions respectively. The impeller region is meshed with 78x140x30 hexahedral elements along pitch, meridional, and span-wise directions respectively. The model uses segregated solver in which all the equations are solved sequentially along with the second-order upwind discretization scheme for convective terms in momentum, energy, turbulence kinetic energy and the rate of dissipation of turbulent kinetic energy. A linear interpolation scheme is used to estimate the cell face pressure as the average of all the pressure values in the adjacent cells. The density interpolation scheme is based on upwind interpolation of density at the cell faces for compressible flow calculations. The pressure-velocity coupling method is based on SIMPLE algorithm and a point implicit Gauss-Seidel linear equation solver is used in conjunction with the algebraic multigrid (AMG) method to solve the resultant scalar system of equations for the dependent variable in each cell with a specified convergence limit of 1×10^{-6} .

Fluid flow characteristics in the single blade passage of the centrifugal fan impeller are analyzed in this section. The distribution of pressure and velocity field and its impact on the losses inside the channel are studied. The results presented in this section include implementation of two numerical approaches for turbo modeling, and performance of different turbulence models.

3.1.3.2 Turbulence modeling

A turbulence model study is conducted on the single blade passage of the impeller in order to understand the flow characteristics and pressure losses occurring due to flow separation

and circulatory flows. The different turbulence models considered are the Spalart-Allmaras model, which is a one-equation model; the two-equation model, namely the standard k-ε model; realizable k-ε model with non-equilibrium wall functions, and the RNG model. Since the maximum losses occur at around x/c=0.3 location in meridional direction along the passage, the performance of turbulence models is compared in this region to predict the flow behavior for the base case.

3.1.4 Analysis of flow field

Figure 5 shows the static pressure distribution for all the turbulence models considered for the base case. Results show similar static pressure distribution on the pressure side of the blade. However, there is a significant variation of static pressure distribution and the size of the low-pressure region on the blade suction side predicted by the different turbulence models. Figure 6 shows the distribution of dynamic pressure at the blades leading edge.

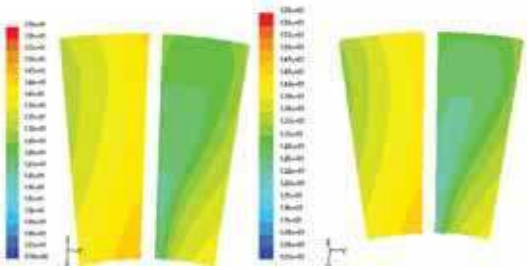

(a)Spalart Allmaras model

(b) Standard k-ε model

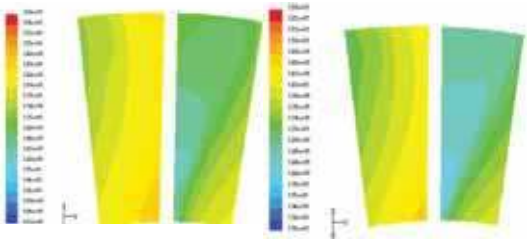

(c) Realizable k-ε model

(d) RNG model

Fig. 5. Static pressure at x/c = 0.3

It can be seen that all the models predict large recirculation regions on the blade suction side. On the pressure side of the blade, low-pressure region is developed at the hub-pressure side corner and on the suction side at the suction-casing corner. The vector plot of relative velocity vectors in the meridional view, as presented in Figure 7, reveal large areas of low velocity regions on the blade suction side. The flow separation region is developed close to suction-casing corner due to the flow turning from the axial direction to radial direction. It can be seen that the RNG model predicts larger area of flow separation compared to other turbulence models considered.

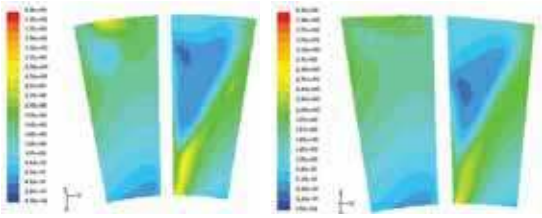

(a)Spalart-Allmaras model

(b)Standard k-ε model

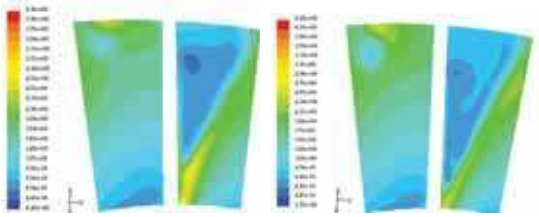

(c) Realizable k-ε model

(d) RNG Method

Fig. 6. Dynamic pressure distribution at x/c = 0.3

Plots of relative velocity vectors both at the critical section and at the mid-span region are presented in figures 7 and 8.

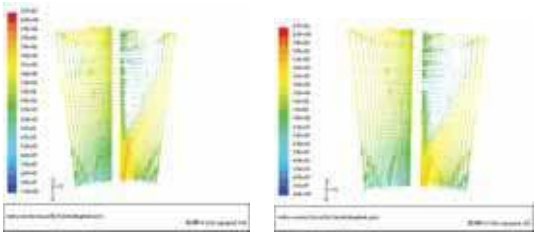

(a) Spalart Allmaras model

(b) Standard k-ε model

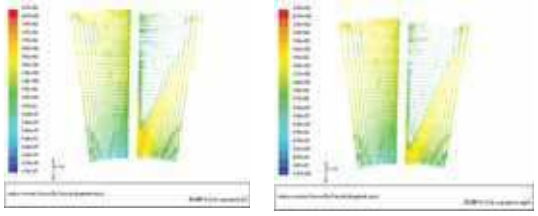

(c) Realizable k-ε model

(d) RNG model

Fig. 7. Relative velocity vectors magnitude at x/c = 0.3

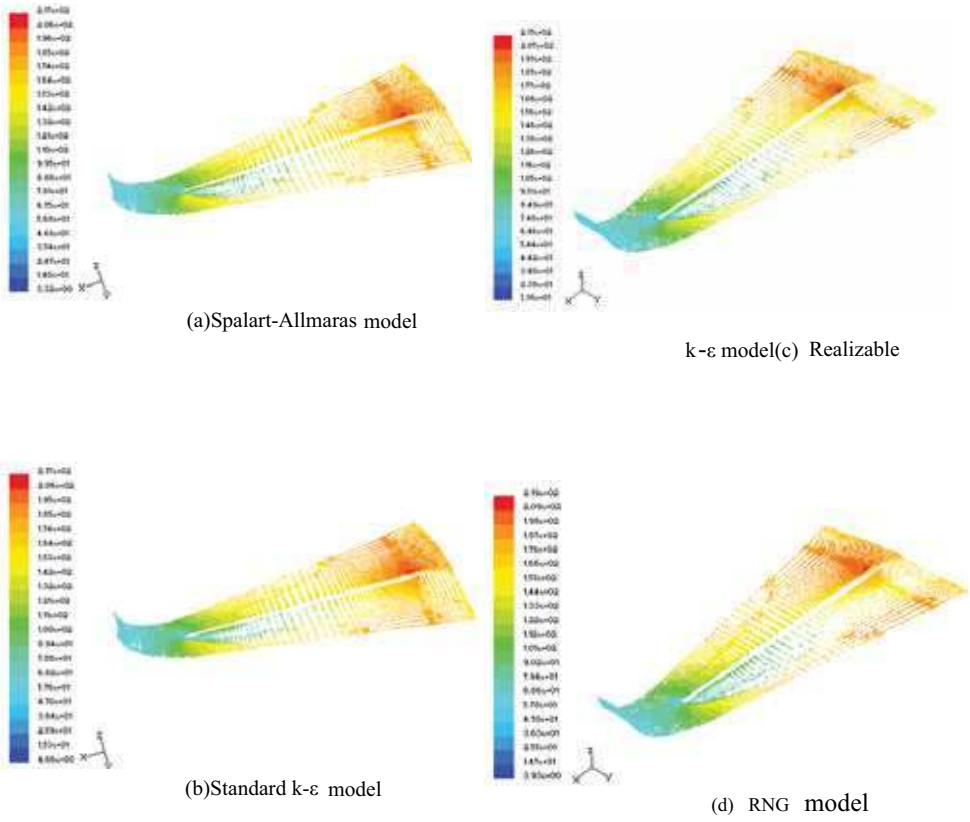

Fig. 8. Relative velocity vectors magnitude at mid-span

The plot of velocity vectors at mid-span of the passage, as given by Figure 8, shows flow separation on the blade suction side close to the leading edge. The realizable k-ε model and RNG model predict higher flow separation region compared to the Spalart-Allmaras and the standard k-ε models. Figure 9 shows the shadow graph plots of the normalized turbulent kinetic energy distribution along the blade passage. It can be seen from the contour plots of turbulent kinetic energy that the turbulence is stronger on the blade suction side due to the presence of higher momentum fluid. The realizable k-ε model and the RNG model show a better resolution of the turbulence compared to the standard k-ε model.

Results in figure 10 at the mid-span show that the turbulence structure predicted by the RNG model spreads from the blade leading edge on suction side to about 70% of the passage distance which is higher than the structure predicted by the realizable k-ε model and the standard k-ε model, but the intensity of the turbulence magnitude predicted decreases from the standard k-ε model to realizable k-ε model and to the RNG model.

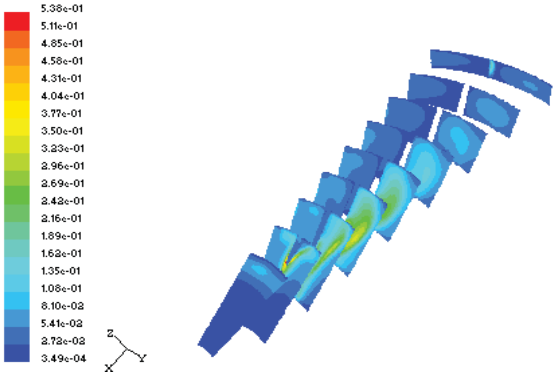

(a)Standard k - ε

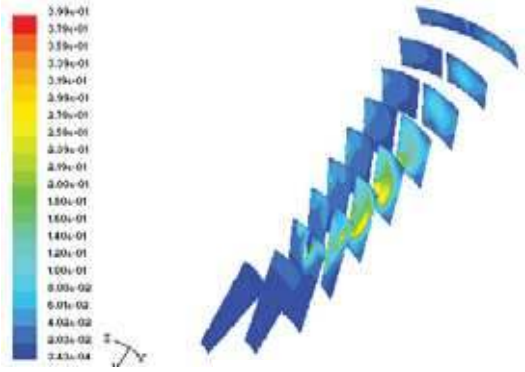

(b) Realizable k-ε model

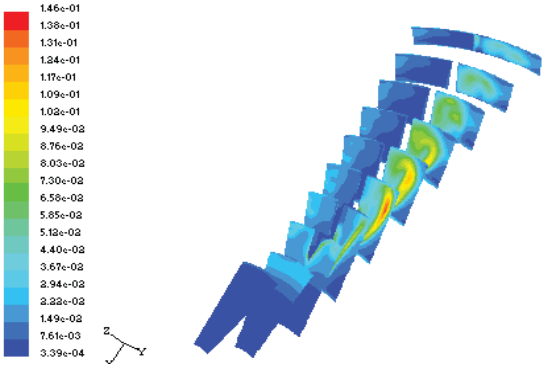

(c) RNG

Fig. 9. Normalized turbulent kinetic energy contours along the passage

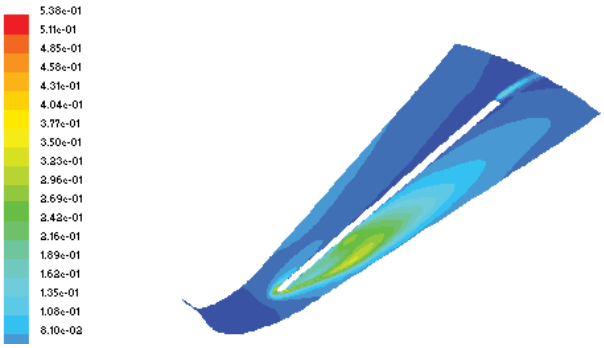

(a) Standard k-ε

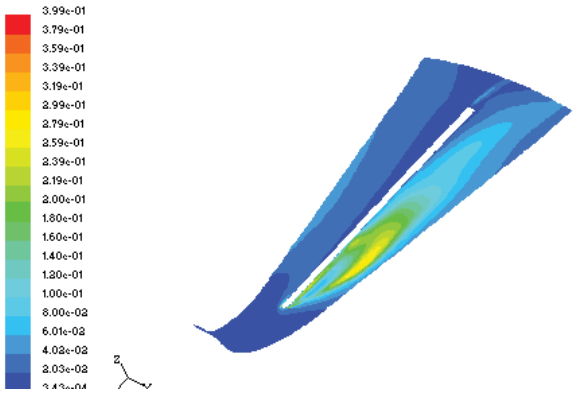

(b) Realizable k-ε

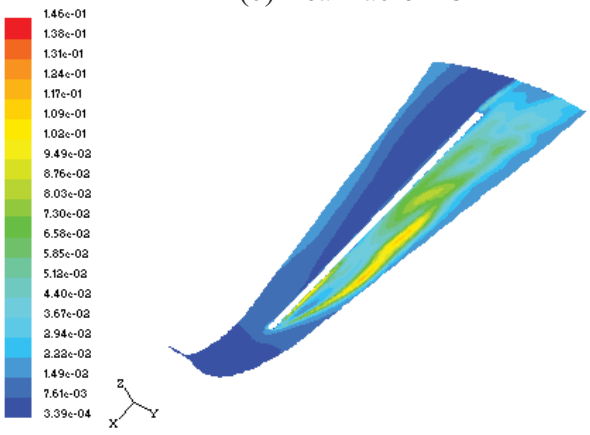

(c) RNG

Fig. 10. Normalized turbulent kinetic energy contours at mid-span

The variation of area-averaged normalized turbulent kinetic energy and dissipation rate is shown in Figures 11 and 12 respectively. The turbulent dissipation rate is normalized with respect to the inlet velocity and the blade chord length.

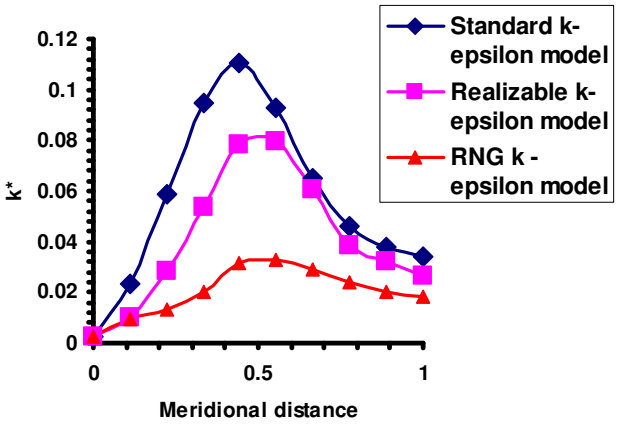

Fig. 11. Variation of normalized turbulent kinetic energy along the passage

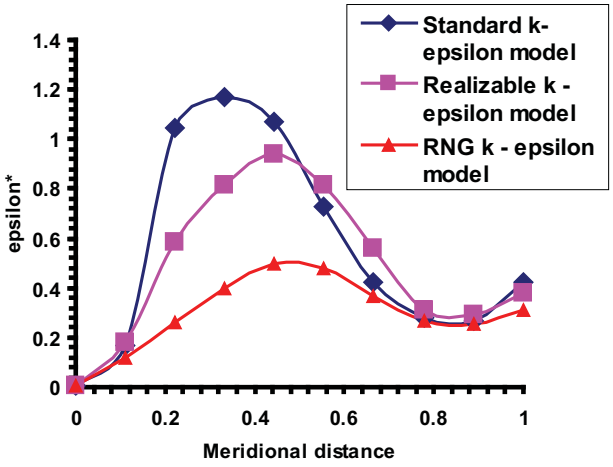

Fig. 12. Variation of normalized dissipation rate along the passage

From figure 11 it is observed that the turbulence kinetic energy develops from the inlet and rises to a peak value at approximately the center of channel. The standard k-ε model over predicts the turbulent kinetic energy more than the other Realizable and RNG models. From figure 12 it can be seen that the realizable k-ε model predicts less dissipation rate than the standard k-ε model because the transport equation for dissipation rate is based on the dynamic equation of mean square vorticity fluctuation. The RNG model predicts the least dissipation rate of the other two turbulent models since it contains additional terms in the

transport equation for k and ε, which are more suitable for flows with high streamline curvature and high rapid strain rate.
Following are the conclusions of the study:

1. The computational model demonstrated the secondary flow or slip losses in blade passages due to varying velocity gradient between the blade pressure side and suction side.
2. The RNG turbulence model gave more detailed resolution of flow separation and recirculation in the intake region. However, in terms of total pressure rise, the results predicted by the RNG model and the standard κ-ε models were within 0.6%.
3. Further design analysis of centrifugal fan impeller can be performed using standard κ-ε model along with standard wall function to resolve near wall region.

3.2 Case –II: numerical simulation of turbulent fluid flow over a surface- mounted

Fluid flow and heat transfer over a block in square tubes; ducts and channels have an extensive application in electronics cooling and heat exchanger design. The objective of this work is to study three-dimensional turbulent flow over a surface mounted block in a channel with adverse pressure gradient giving rise to flow separation and reattachment. The study focuses on evaluating different turbulence models for simulating turbulence and flow statistics using FLUENT commercial code. Computational solution is compared with existing experimental data in the literature. A parametric study is also conducted to analyze the flow separation, turbulence statistics and pressure coefficient with varying geometrical parameters over a range of Reynolds number. Figure 1 gives the schematic representation of the problem.

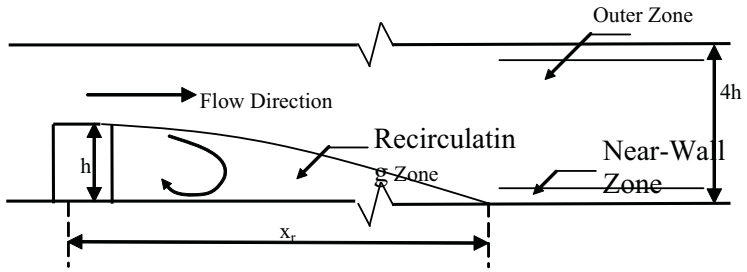

Fig. 13. Schematic representation of the problem

3.2.1 Governing equations

RNS flow equation with Reynolds stresses expressed via the eddy viscosity concept has been used. Turbulence closure model considered are 1. High Reynolds number $\kappa-\varepsilon$ turbulent model, 2. The RNG $\kappa-\varepsilon$ model, 3. The Reynolds Stress model.

3.2.1.1 Mesh generation

Volumetric mesh with regulated spacing of the control volume is done using mapped meshing technique as shown in figure 14. A soft non-uniform grading scheme is used for edge meshing. Near wall meshing is performed based on the distance established by wall function treatment. Mesh size distribution nears wall is selected based on satisfying wall function requirement and keeping the values of y^+ along the wall surfaces within 30 to 60.

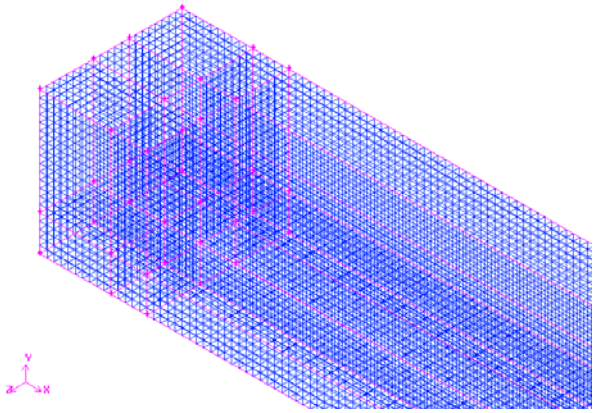

Fig. 14. Mesh size distribution

Core mesh is refined until the percentage relative error of the centerline velocities decreases and the maximum percentage relative error is below 0.003413 %. Typical mesh of the model is with 201895 cells, 62876 faces, 222604 nodes, 1 cell zones, and 5 face zones. Mesh is refined along x, y and z directions and the velocity variation is studied for different kinds of mesh generated. The element used in the mesh generation is an 8-node hexahedron volume element. In order to validate the accuracy of turbulence models, results are compared with the experimental data obtained from the test case of Kasagi and Matsunga [1993]. The test case is the flow over a backward facing step involving adverse pressure gradient and boundary layer separation. The schematic representation of the flow filed is show in the figure 15. A steam-wise fully developed flow passes over the backward-facing step with an expansion ratio of 1.504. The hydraulic Reynolds number flow as defined by the step height is 5540. The experiment was conducted in a closed-loop water channel flow facility. Numerical simulations with different turbulent model are compared with the experimental data.

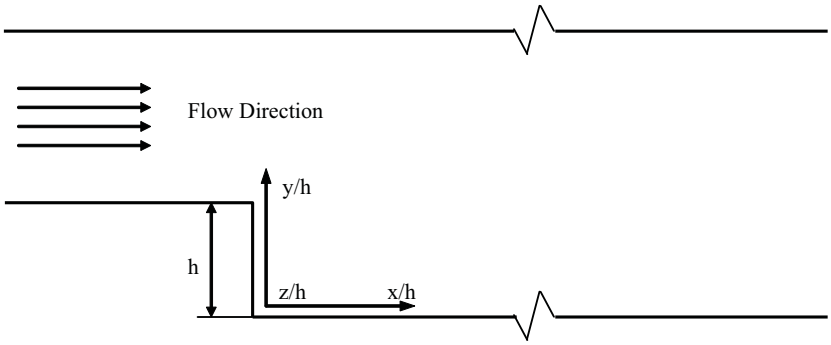

Fig. 15. Schematic representation of the experiment conducted by Kasagi and Matsunga [1993]

The non-dimensional x-velocity profile at the center of the channel at different x-locations is shown in the Fig. 16. As it can be seen that the velocity distribution at a distance of 0.0244h is closely predicted by all four models. However prediction is exceptionally accurate for Reynolds stress model. Since the flow in this region is primarily a core turbulent flow.

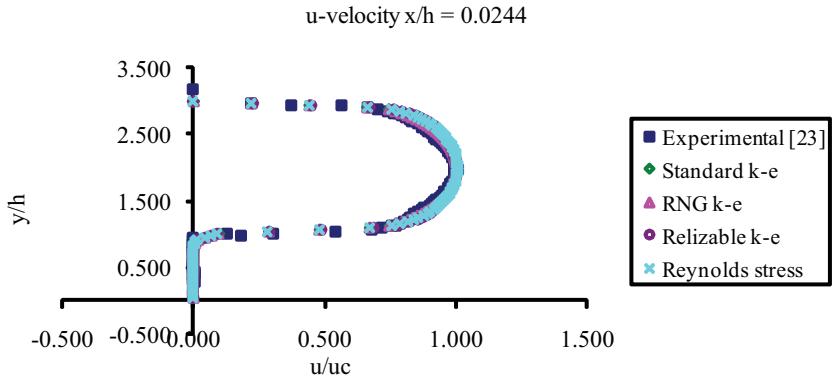

(a) Comparison at x = 0.0244h

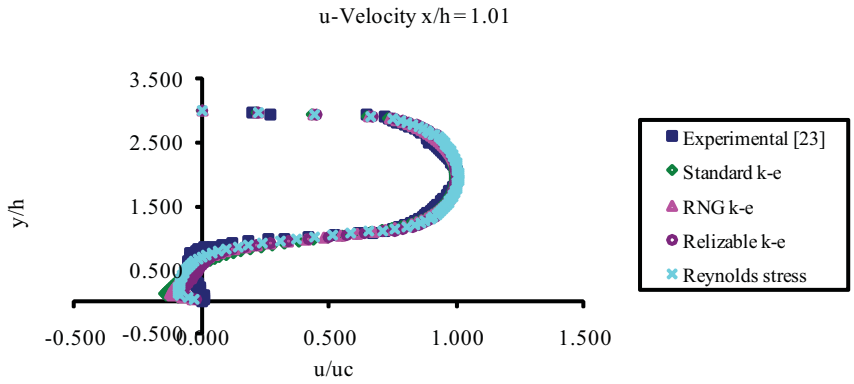

(b) Comparison at x=1.01h

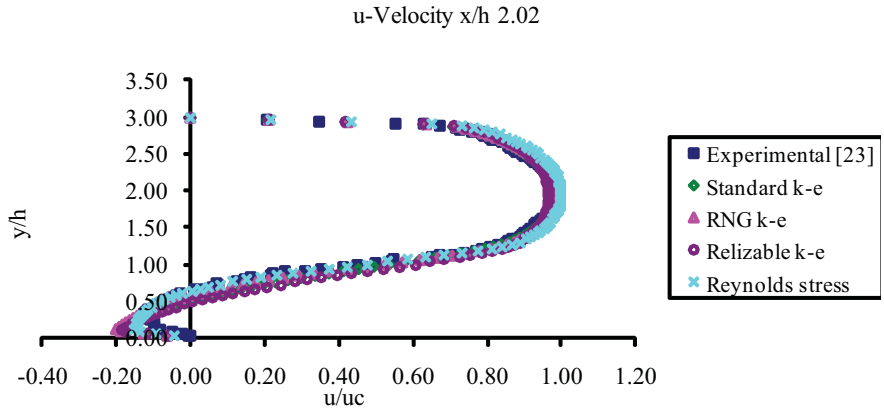

(c) Comparison at x = 2.02h

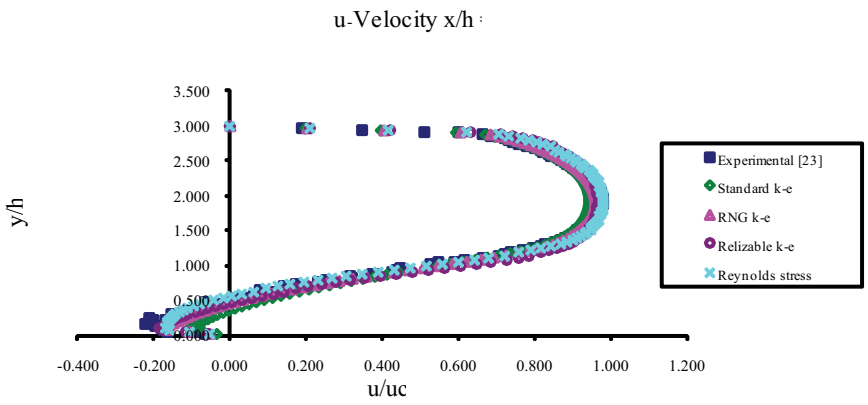

(d) Comparison at x = 3.00h

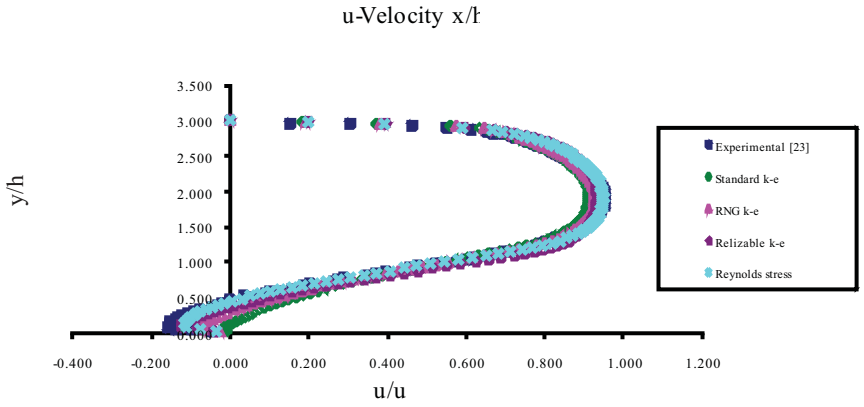

(e) Comparison at x=4.02h

Fig. 16. Comparison with experimental data

Fluid flow after the step height is highly unsteady for many reasons. Distortion of boundary layer, adverse pressure gradient, normal shear stress and, secondary or backflow are some of the reason. At x/h = 1.01, a reverse flow is observed (as shown in Figure: 16b). All the turbulent models predict the reversed flow. But, magnitudes of the reversed flow are different form the experimental data. This portion fall under the core of the recirculation zone, where maximum deviation between the numerical and experimental data is observed. As we move away from this region representation of the recirculation region is more accurate as discussed in the following section. The intensity of the back flow decreases as we traverse along the flow direction. The secondary flow and effect of swirl on the flow decrease. In figures 16c-e, the x component of velocity at different locations in the recirculation is compared. The deviation form the experimental data decreases as the flow becomes to stabilize. A better prediction is observed as we move away from the wall and the recirculation zone. The major contribution of this may be due to the numerical computation

given by different turbulent closure model. The seven equations, Reynolds stress model predicts better results in comparison with the other turbulent models used.

Velocity contours plots at the center plane of the flow regime are presented for the range of Reynolds number in Fig. 17. Two critical points are observed. The obstruction in the direction of the fluid flow causes in an increase in the thickness of boundary layer followed by the point of detachment. The recirculation of the flow right after the obstruction is evident from the figures. The number of contours in the recirculation zone increases as the Reynolds number increase, signifying the increase in the recirculation strength.

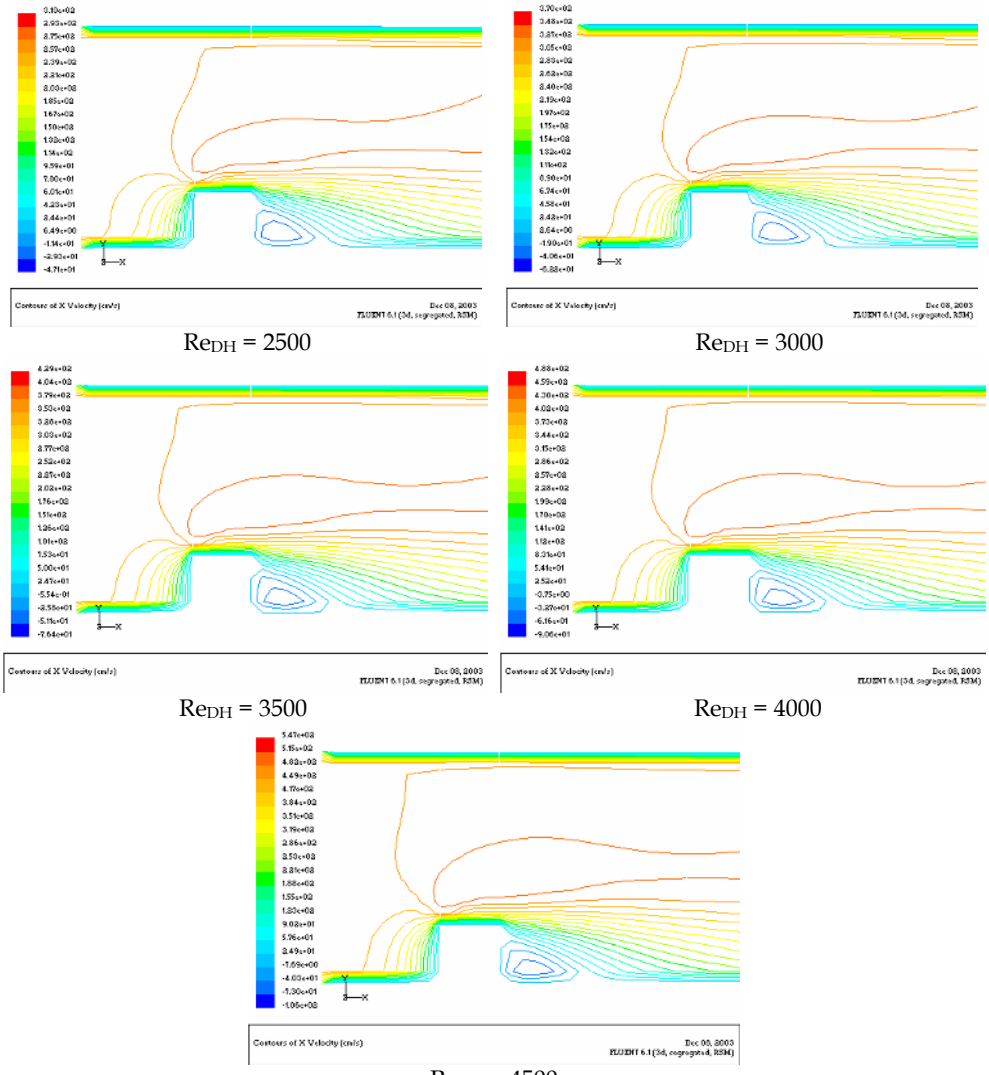

Re_{DH} = 2500 Re_{DH} = 3000

Re_{DH} = 3500 Re_{DH} = 4000

Re_{DH} = 4500

Fig. 17. Velocity contour plot at the center plane

The pressure coefficient (C_P) along the flow direction at the center of the flow is plotted for different Reynolds numbers ranging from 2500-4500 in the Fig. 18. The detachment of the boundary layer causes adverse pressure gradients. C_p decrease as the velocity at the inlet increases. With the increase in $Re_{DH,}$ the pressure drop increases. The comparison of static pressure at x =1.75 cm on the center plane with different Reynolds numbers is shown in Fig. 18. If the pressure gradient continues to increase, the velocities eventually come to zero and reversal of the flow will occur (backflow). To compensate the effect of the pressure gradient, the flow velocity decelerates to maintain the continuity of the domain

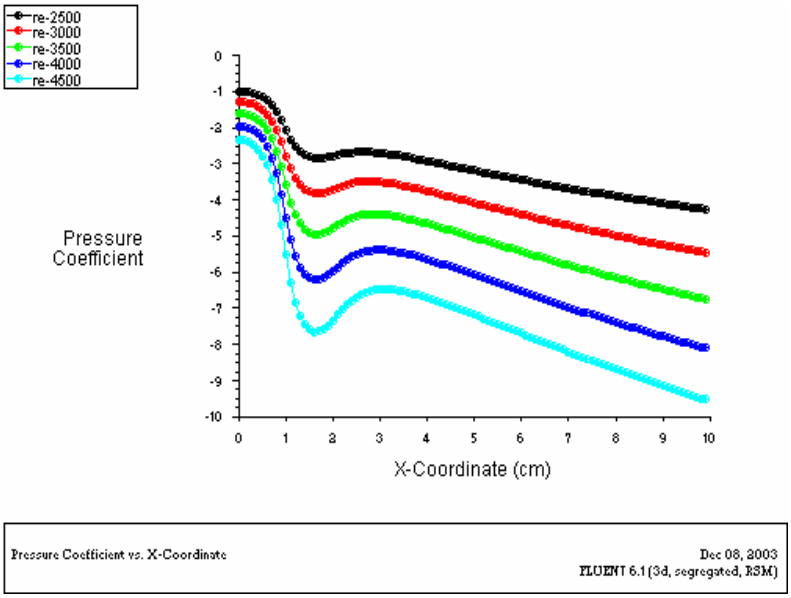

Fig. 18. Comparison of C_P with different Reynolds numbers

Velocity vector plots are presented in Fig. 19. It is evident that the size of the recirculating eddy as well as the magnitude of reversed flow (i.e. the negative velocities) increases as the Reynolds number increases.

Backflow is also a result of turbulent statistics moving upstream for some distance, then reversing and being convected downstream. The rate at which this phenomenon occur increase as the detachment location is approached. Velocity vector along the x-direction, at the mid-section of the block along the flow direction, for different Reynolds numbers are shown in the following Fig. 20. As the Reynolds number increases the swirl velocity and the eddy formation around the block dramatically increases.

The turbulent flow consists of production, convection, diffusion and, dissipation of turbulent energy. Dissipation and production play crucial role on turbulent energy in order to minimize the pressure gradient in the region far away from the wall. In the recirculating region, turbulent intensity increases as the Reynolds number increases. The turbulent viscosity, kinetic energy and, its dissipation rate along the y-axis at the x=1.75 cm on the center plane are plotted in the Fig. 21. In the recirculating region, viscosity decreases as the Reynolds number increases. It can be observed that as the velocity of the fluid field increase,

the pressure in the recirculating zone decreases and the turbulent properties such as turbulent kinetic energy, its dissipation rate increases, but the turbulent viscosity decreases.

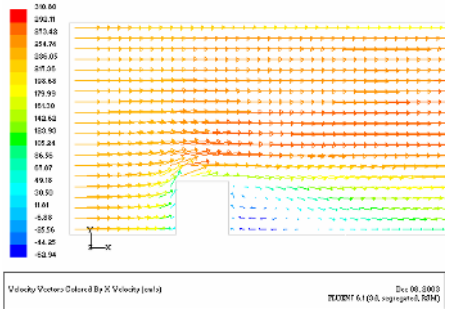

Re_d = 2500

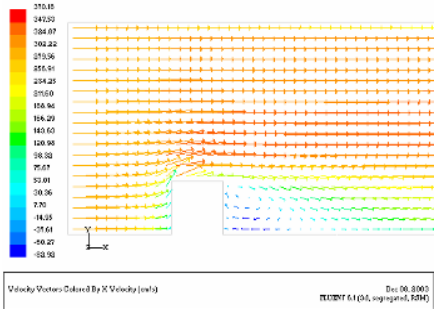

Re_{DH} = 3000

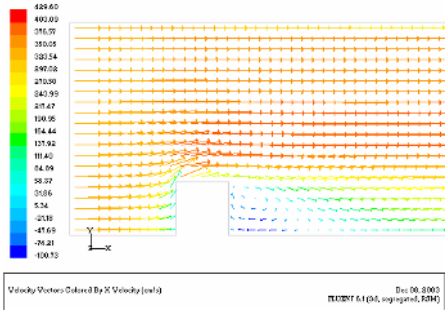

Re_d = 3500

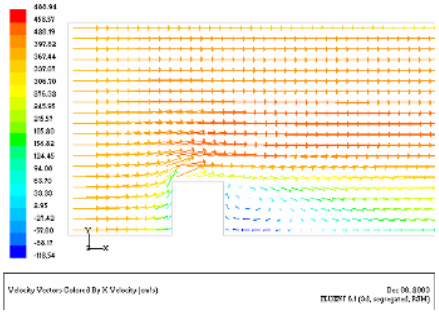

Re_{DH} = 4000

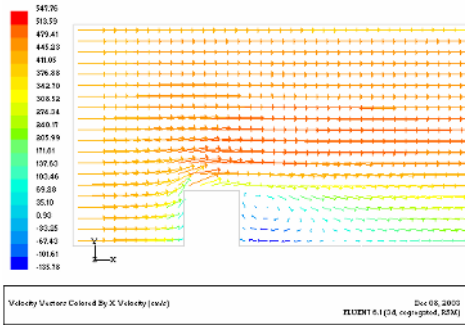

Re_{DH} = 4500

Fig. 19. Velocity vectors along the x-direction at the center plane

The reattachment length (x_r). is the distance from the point of detachment of the fluid from solid to the point of attachment. The change in reattachment over varying Reynolds number is studied. The reattachment length is a critical quantity because the re-development of the

boundary layer and pressure recovery starts at this point. Since the maximum reattachment is observed at the center due to the effect of the y and z velocities the center plane is chosen. Figure 22 shows that the reattachment point moves along the flow direction with increase in Reynolds number.

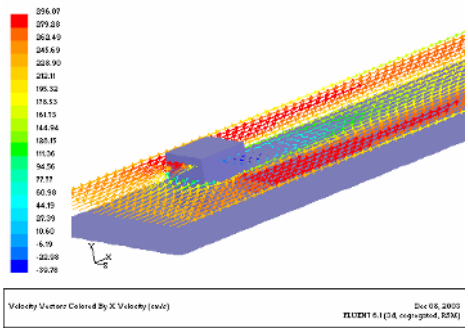

Re_{DH} = 2500

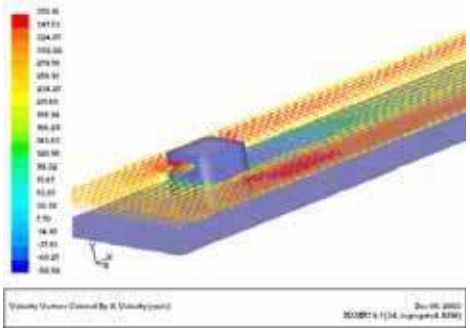

Re_{DH} = 3000

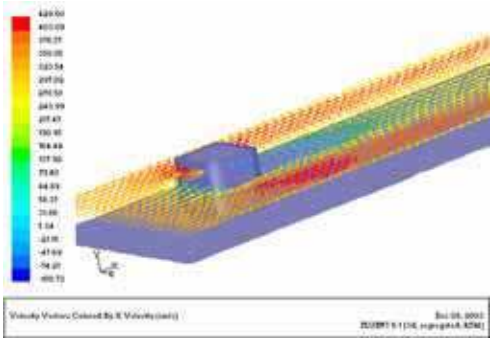

Re_{DH} = 3500

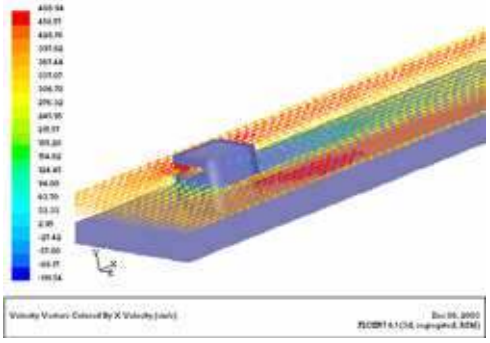

Re_{DH} = 4000

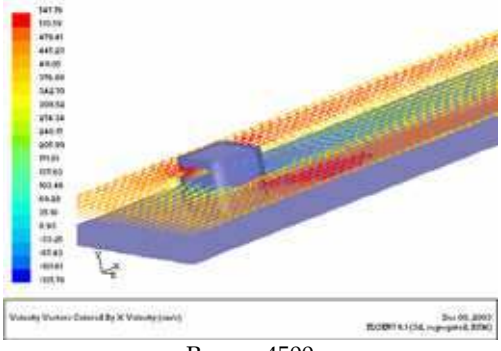

Re_{DH} = 4500

Fig. 20. Velocity vectors around the block

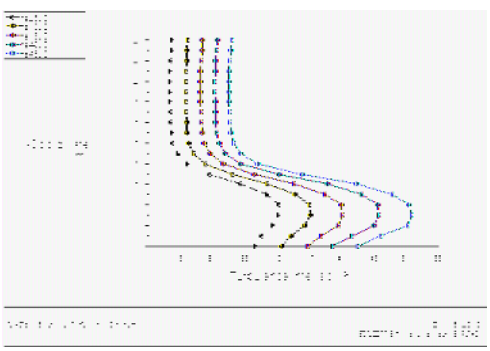

Turbulent intensity at x = 1.75 cm

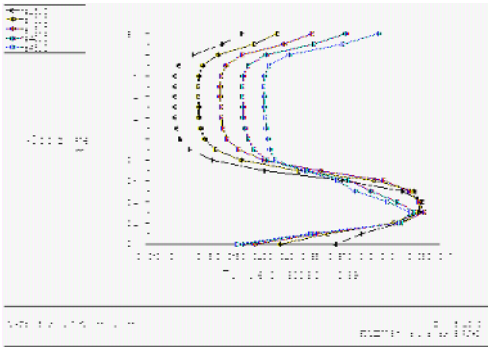

Turbulent viscosity at x =1.75 cm

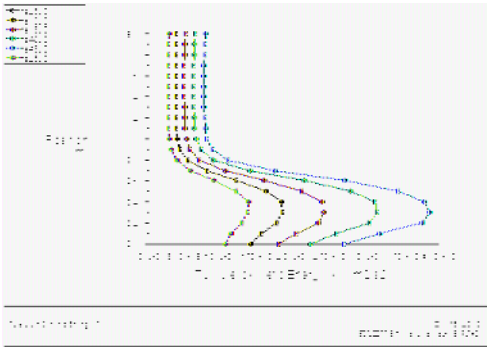

Kinetic energy rate

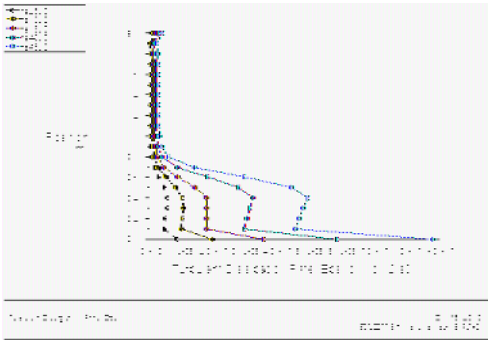

Dissipation rate

Fig. 21. Comparison of turbulent quantities at x = 1.75 cm with varying Reynolds number

4. Conclusion

A description of computational fluid dynamics analysis methods for turbulent fluid flow in number engineering problems is discussed. While a brief description of different turbulent modeling approaches such as Reynolds Averaged Nervier-Stokes (RANS) equations, Large Eddy Simulations (LES) and Direct Numerical Simulation (DNS) is given, a more detail consideration is given to the of RANS method with turbulence closure models and to the computational challenges such as the selection of appropriate turbulence closure model, wall function treatment, inlet turbulent and application to number of engineering problems. Four different classes of turbulence closure models such as i) algebraic zero-order equation $k-\varepsilon$ turbulence models including low Reynolds number models, iv) $k-\omega$ turbulence models, and v) Reynolds Stress Model (RSM) and. their selection of an appropriate model for a specific application is considered. Examples are drawn from practical industrial applications, and results from extensive numerical experimentations and validations with experimental data are presente3d to demonstrate the challenges in turbulent flow simulations.

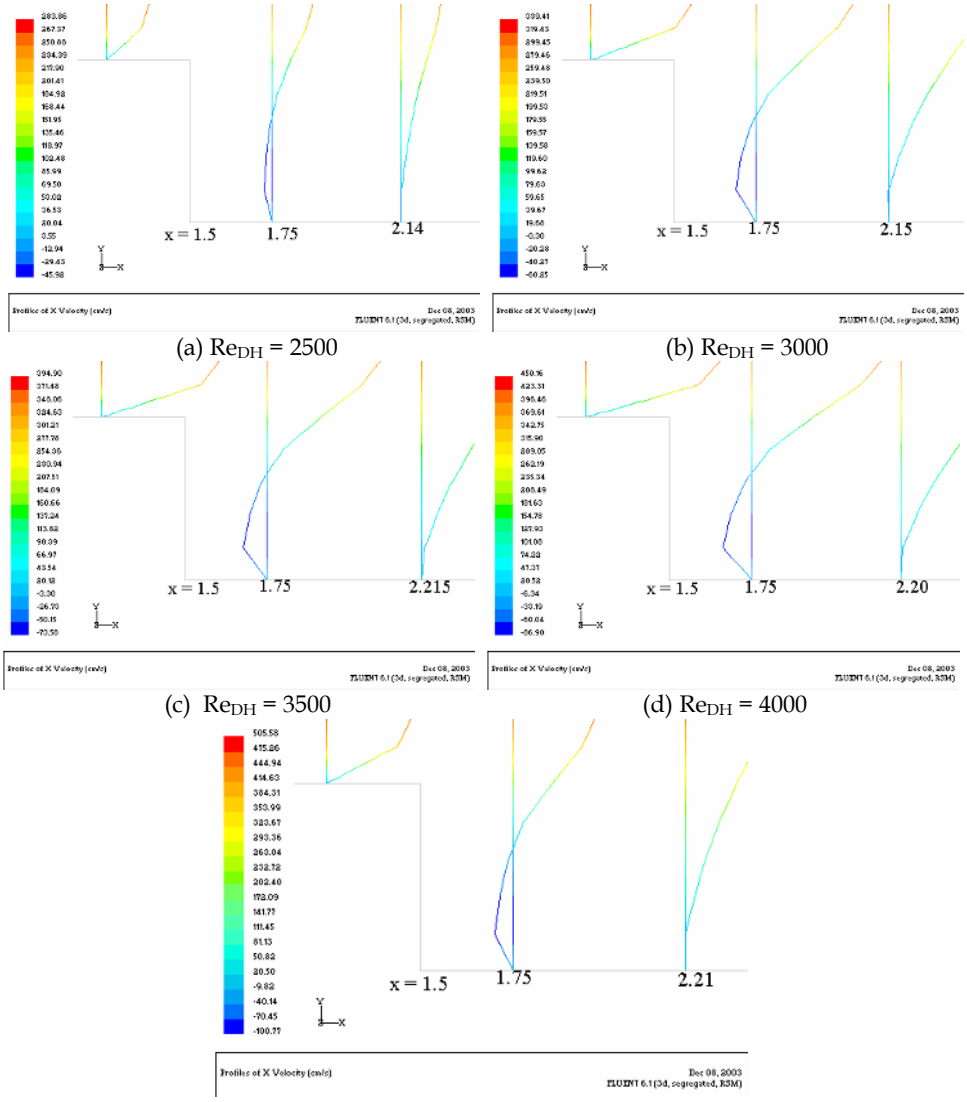

Fig. 22. Flow separation and reattachment at different Reynolds number.

5. References

Agonafer, D., Moffatt, D. F. (1990). Numerical Modeling of Forced Convection Heat Transfer for Modules Mounted on Circuit Boards. *ASME*, Vol. 112, pp. 112-333.

Asaka, Y. and Mohammad Faghri (1995). Prediction of Turbulent Heat Transfer in the Entrance of an Array of Heated Blocks using Low-Reynolds-Number k- ε model. *Numerical Heat Transfer*, Part A, 28:263-277.

Choudhury, D. (1993). Introduction to the Renormalization Group Method and Turbulence Modeling. Fluent Inc. Technical Memorandum TM-107.

Chung, B. T. F., & Li, H. H. (1992). Forced Convective Cooling Enhancement of Electronic Modules through a Double Layer Cavity Design. *Fundamentals of Forced Convection Heat Transfer*. ASME, Vol. 210.

Cotton, M. A., Jackson, J. D. (1989). Vertical Tube Air Flow in the Turbulent Mixed Convection Region Calculated using a Low-Reynolds-Number k- ε Model. *International Journal of Mass and Heat Transfer*, Vol. 33, No. 2, pp. 275-286.

Deb P. and Majumdar Pradip, Direct Numerical Simulation of Mixing of a Passive Scalar Decaying Turbulence, *Proceedings of the 1999 International Mechanical Engineering Congress and Exhibition* (IMECE), Nov. HTD-Vol.364-3, pp. 299- 306, 1999.

Deb, P and Pradip Majumdar, Numerical Investigation of the Effect of Variable Viscosity on Decaying Turbulence Flow Field using DNS technique Paper NoNHTC2000-12085. *Proceedings of NHTC'00, 34th ASME National Heat Transfer Conference*, Pittsburgh, August, 2000

Deb, Prasanta and Majumdar, P., (2000), Turbulence Flow and Heat Transfer Over Heated Modules for a Wide Range of Reynolds Numbers and Module Size, *Journal of Electronics Manufacturing*, Vol. 10, No. 4, pp. 263-269, 2000.

Deb, Prasanta and Pradip Majumdar. Numerical Investigation of Fluid Flow and Heat Transfer Over Distributed Heated Modules with the Standard k-ε model and a low Reynolds Number Model, *Proceedings of the 33rd ASME National Heat Transfer Conference*, Albuquerque, NHTC'99, pp. 1-7, 1999.

Dogruoz, M., B. CFD Benchmark Testing of Selected Laminar Flow Problems. Department of Aerospace and Mechanical Engineering, Experimental and Computational Heat Transfer Group, The University of Arizona. Available [Online]: <http://w3.arizona.edu/~thermlab/>

Dutta, S. and S. Acharaya (1993). Heat Transfer and Flow Past a Backstep with the Nonlinear k- ε Turbulence Model and the Modified k- ε Turbulence Model. *Numerical Heat Transfer*, Part A, Vol. 23, pp. 281-301.

Eswaran, V and Pope, S. B, (1988), Direct Numerical Simulations of the Turbulent Mixing of a Passive Scalar, *Physics of Fluids*, v. 31, p.506.

Gibson, M. & Launder, B. (1978). Ground Effects on Pressure Fluctuations in the Atmospheric Boundary Layer, *Journal of Fluid Mech.* pp. 491-511.

Gibson, M. and Launder, B. (1978). Ground Effects on Pressure Fluctuations in the Atmospheric Boundary Layer, *Journal of Fluid Mech.* pp. 491-511.

Kang, S., Hirsh, Sh. (1999) Numerical investigation of the three dimensional flow in NASA low speed centrifugal compressor impeller. *Proceedings of the Fourth International Symposium on Experimental and Aerothermodynamics of Internal Flows*, Germany, Aug. 31 – Sept. 2, 1999.

Kasagi, N and Matsunaga, A. (1995). Three-dimensional Particle-tracking Velocimetry Measurement of Turbulence Statistics and Energy Budget in a Backward-facing Step Flow. *International Journal of Heat and Fluid Flow*, Vol. 16, pp. 477-485.

Kasagi, N., & Matsunaga, A. (1993). Turbulence Measurement in a Separated and Reattaching Flow Over a Backward-Facing Step with the Aid of Three-Dimensional Particle Tracking Velocimetry, *Journal of Wind Engineering and Industrial Aerodynamics*, Vol. 46 & 47, pp. 821-829.

Lakshminarayana, B. (1996) *Fluid Dynamics and Heat Transfer of Turbomachinery*, John Wiley & Sons, Inc.

Larosiliere, L.M., Skoch, G.J., Prahst, P.S. (1997) Aerodynamic synthesis of a centrifugal impeller using CFD and measurements. NASA TM – 107515, AIAA- 97-2878, July 1997.

Launder, B. (1989). Second-Moment Closure, *International Journal of Heat and Fluid Flow*, Vol. 10, pp. 282-300.

Launder, B. (1989). Second-Moment Closure, *International Journal of Heat and Fluid Flow*, Vol. 10, pp. 282-300.

Launder, B., E. and Spalding, D. B., (1974). Numerical Computation of Turbulent Flows, *Comp. Methods in Appl. Mech, and Engg*., 3, 269-289.

Launder, B., Reece, G. and Rodi, W. (1975). Progress in the Development of a Reynolds-Stress Turbulence Closure, *International Journal of Heat and Fluid Flow*, Vol. 68, pp. 537-566.

Launder, B., Reece, G. and Rodi, W. (1975). Progress in the Development of a Reynolds-Stress Turbulence Closure, *International Journal of Heat and Fluid Flow*, Vol. 68, pp. 537-566.

Launder, B.E and Spalding, D.B. (1972) *Lectures in Mathematical Models of Turbulence*, Academic Press, London, England.

Lehmann, G. L., Wirtz, R. A. (1985). The Effect of Variation in Stream-wise Spacing and Length on Convection from surface Mounted Rectangular Components. *ASME Winter Annual Meeting*, Denver, HTD Vol. 48, pp. 39-47.

Majumdar, P., and Deb, P. (2003). Computational Analysis of Turbulent Fluid Flow and Heat Transfer over an Array of Heated Modules using Turbulence Models. *Numerical Heat Transfer*, Part A, Vol. 43, pp. 1-21.

Majumdar, P., Computational Methods for Heat and Mass Transfer, Taylor & Francis Publisher, 2005.

Majumdar, Pradip and Prasanta D., (2000), Numerical Prediction of Fluid Flow and Heat Transfer Over Heated Modules using the Standard k-ε Model and Low Reynolds Number Models Paper No. NHTC2000-12257, pp- 1-8, *Proceedings of the NHTC'00, 34th ASME National Heat Transfer Conference*, Pittsburgh, August, 2000

Mawlood, K., Asrar, W., Omar, A., and Basri, S. (2002). Flow Past a Backward-Facing Step: Fourth-Order Compact Finite-Difference Results. *32nd AIAA Fluid Dynamics Conference and Exhibit*, pp. 24-25

Piller, M., Nobile, E. (2002). Direct Numerical Simulation of Turbulent Heat Transfer in a Square Duct. *International Journal for Numerical Methods for Heat & Fluid Flow*, Vol. 12, pp. 658-686.

Rai, M. M and Moin, P., (1991), Direct Simulation of Turbulent Flow Using Finite Difference Schemes, *J Comp. Physics*, Vol. 96, p. 15, 1991.

Rogallo, R. S., (1981), Numerical Experiments in homogeneous Turbulence, NASA Report NO: N81-31508.

Shih, T. and Liou, W. (1995). A New $k-\varepsilon$ Eddy- Viscosity Model for High Reynolds Number Turbulent Flows – Model Development and Validation. *Computers Fluids*. pp. 227-238.

Wagner, C., T. Huttl and P. Sagaut, Large-Eddy Simulation for Acoustics, Cambridge University Press, 2007

Wilcox, David C. (1993). Turbulence Modeling for CFD. DCW Industries, Inc. La Canada, California.

Xiadong, B., Xudong, T., Zhichi, Z. (2000) Application of numerical simulation of flow field of centrifugal impellers for fan design. *Tsinghua Science and Technology*, Vol.5, No.1, pp. 82-88.

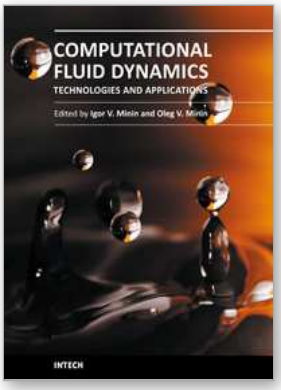

Computational Fluid Dynamics Technologies and Applications
Edited by Prof. Igor Minin

ISBN 978-953-307-169-5
Hard cover, 396 pages
Publisher InTech
Published online 05, July, 2011
Published in print edition July, 2011

This book is planned to publish with an objective to provide a state-of-art reference book in the area of computational fluid dynamics for CFD engineers, scientists, applied physicists and post-graduate students. Also the aim of the book is the continuous and timely dissemination of new and innovative CFD research and developments. This reference book is a collection of 14 chapters characterized in 4 parts: modern principles of CFD, CFD in physics, industrial and in castle. This book provides a comprehensive overview of the computational experiment technology, numerical simulation of the hydrodynamics and heat transfer processes in a two dimensional gas, application of lattice Boltzmann method in heat transfer and fluid flow, etc. Several interesting applications area are also discusses in the book like underwater vehicle propeller, the flow behavior in gas-cooled nuclear reactors, simulation odour dispersion around windbreaks and so on.

How to reference
In order to correctly reference this scholarly work, feel free to copy and paste the following:

Pradip Majumdar (2011). Computational Fluid Dynamics Analysis of Turbulent Flow, Computational Fluid Dynamics Technologies and Applications, Prof. Igor Minin (Ed.), ISBN: 978-953-307-169-5, InTech, Available from: http://www.intechopen.com/books/computational-fluid-dynamics-technologies-and-applications/computational-fluid-dynamics-analysis-of-turbulent-flow

INTECH
open science | open minds

InTech Europe
University Campus STeP Ri
Slavka Krautzeka 83/A
51000 Rijeka, Croatia
Phone: +385 (51) 770 447
Fax: +385 (51) 686 166
www.intechopen.com

InTech China
Unit 405, Office Block, Hotel Equatorial Shanghai
No.65, Yan An Road (West), Shanghai, 200040, China
中国上海市延安西路65号上海国际贵都大饭店办公楼405单元
Phone: +86-21-62489820
Fax: +86-21-62489821

© 2011 The Author(s). Licensee IntechOpen. This chapter is distributed under the terms of the Creative Commons Attribution-NonCommercial-ShareAlike-3.0 License, which permits use, distribution and reproduction for non-commercial purposes, provided the original is properly cited and derivative works building on this content are distributed under the same license.